A study on the hydroacoustic characterisation of a cavitating propeller by dynamic adaptive mesh refinement technique

Çağatay Sabri Köksal [a,b,*], Batuhan Aktas [b], Mehmet Atlar [b], Emin Korkut [a]

[a] *Faculty of Naval Architecture and Ocean Engineering, Istanbul Technical University (ITU), Istanbul, Turkey*
[b] *Naval Architecture, Ocean and Marine Engineering, University of Strathclyde (UoS), Glasgow, Scotland, United Kingdom*

ARTICLE INFO

ABSTRACT

Underwater radiated noise (URN) of a marine propeller has received significant interest in recent decades due to its implications on marine fauna. Therefore, an accurate prediction of URN at an early stage of the propeller design is becoming imperative. This study presents a numerical investigation into the noise prediction of a marine propeller, including cavitation and a comparison with experimental test results obtained from the URN database from the King's College D (KCD) standard propeller series. Amongst the propellers tested in the series, the member KCD-193 was chosen to scrutinise in this study due to the significant variance of the cavitation types experienced by this propeller member and consequent characteristic variations observed in its URN spectral response. Numerical URN predictions of different flow conditions, represented by the advance coefficient and cavitation number, were conducted to investigate their effects on the noise spectrum. These predictions were compared with the experimental results to enable interpretation of the impact of various aspects of the simulation on URN prediction accuracy. In this investigation, one of the most prominent noise sources, tip-vortex cavitation (TVC), was identified as a critical aspect that needs to be captured by the numerical simulations for accurate URN predictions using CFD simulations. The influence of TVC on the spectrum was observed to be significant. The inception and stable presence of TVC dominated the frequency response of the broadband hump. In order to address this, a systematic adaptive mesh refinement strategy was implemented based on the vortex criterion to solve the flow characteristics in the propeller slipstream accurately. To further complement this task, a correlation between the cavitation bubble growth and collapse phenomenon by the sensitivity of the broadband hump on the spectrum was established based on the experimental results. The central frequency of the broadband hump was observed to vary with the advance coefficient and cavitation number. The reduction in the cavitation number resulted in a shift of this hump towards lower frequencies. The URN level of the hump decreased slightly in the high frequency by the reduction in the advance coefficient and the developing cavitation, demonstrating the cushioning effect on the spectrum. An accurate assessment of the noise spectrum, as far as numerical predictions are concerned, particularly on the broadband hump frequency bandwidth, was directly associated with the resolution of the TVC.

* Corresponding author at: Naval Architecture, Ocean and Marine Engineering, University of Strathclyde (UoS), Glasgow, Scotland, United Kingdom.

E-mail address: cagatay.koksal@strath.ac.uk (Ç.S. Köksal).

1. Introduction

The impact of commercial shipping on marine fauna has become a concern in recent years as shipping volume in ocean transport has increased over the last half-century, increasing various emissions from seagoing vessels [1]. While the initial emphasis was on reducing greenhouse gas emissions, attention has recently been expanded to include the underwater noise produced by commercial ships due to the potential impact on marine life [2]. In response to these concerns, international organisations and their associated committees, such as the International Maritime Organization (IMO) and the Marine Environmental Protection Committee (MEPC), have begun research into underwater radiated noise from commercial shipping, developing potential guidelines and regulations [3,4]. In addition, the European Union (EU) established the Marine Strategy Framework Directive (MSFD) to investigate and implement programmes of measures aimed at achieving or maintaining Good Environmental Status (GES) in the marine environment [5]. In the last decade, several collaborative European Research and Development (R&D) Projects have been conducted to address the issue of URN from commercial shipping. These projects, including SILENV, AQUO, and SONIC, were conducted under the 7th Framework Programme of the European Union (EU) in response to the Oceans'13 call. More recently, the H2020 project SATURN and the LIFE+ project PIAQUO support the development of standards for the specification of source noise levels by equipment suppliers and ship-yards. The most recent but perhaps the most influential thrust to boost the activities on the URN mitigation may be the recent United Nations decision to agree on the legal framework for parts outside national boundaries. The historic treaty is crucial for enforcing 30 × 30 pledges made by the countries at the UN Biodiversity Conference in December 2022 to protect 30 % of the world seas by 2030. A considerable portion of the ship's URN originates from the three principal sources: machinery, propeller, and hull flow noise [6]. Propeller noise, particularly for cavitating propellers, is the most destructive of these sources since the prevailing noise levels can span a broad frequency spectrum [7]. Therefore, the design of a silent ship must minimise propeller noise, particularly cavitation-related noise.

Accurate prediction of URN from marine propellers is important for minimising their impact on marine fauna. While experimental methods are well-established for predicting URN, the discrepancies in the results of the measurements are a matter of fact due to the model basin-based uncertainties [33]. Computational Fluid Dynamics (CFD) solvers are gaining popularity due to the increasing computational power that allows for more accurate simulation of the dominant noise-producing phenomenon, cavitation. With the advancement of computational tools in recent years, the cavitating propeller URN has been predicted using a hybrid CFD approach, which combines an acoustic analogy and a hydrodynamic solver. This approach decouples the flow field and computes the noise sources and sound radiation independently. The Ffowcs Williams Hawkings (FW-H) equation [8], which has applications in both aeroacoustics and hydroacoustics, is the most widely used amongst various acoustic analogies. A novel method for solving the contributions of nonlinear noise sources in the hydroacoustic field is to employ a permeable version of the FW-H equation proposed by Farassat [9]. Several papers have used the permeable FW-H formulation to examine its response to predict the contribution of nonlinear noise sources under non-cavitating and cavitating conditions, despite the fact that there is no general agreement regarding its application in the literature [10–14]. However, because of the previously mentioned modelling challenges with cavitating tip vortices, the cavitating propeller URN is typically predicted by including only the sheet cavitation modelling of the propeller blades [15]. However, it is also believed that the primary cause of the underpredictions in the URN level predictions compared to the experiments and full-scale predictions is their failures to simulate tip vortices and associated cavitation phenomena [16–19,52,53] accurately.

A vortex is a rotational flow that can be typically observed at the ends of lifting foils with finite spans, including propeller tips. The rotation creates a low-pressure zone at the centre of the vortex, also known as the core. The centrifugal forces acting on a vortex are responsible for the decrease in local pressure at its centre. If the vortex motion is powerful enough, the reduction in local pressure at the core will exceed the critical pressure, resulting in a cavitating core, often with entrained nuclei [20,50,51]. This type of cavitation is highly stable for uniform flow conditions and travels unharmed in the slipstream of a propeller or a lifting surface [21]. However, if operating in a non-uniform flow (e.g. a propeller TVC in the wake shadow region of a ship's hull), the vortex may be deformed or even collapse due to the speed of recovery upon leaving the wake shadow region [22]. Such dynamics are frequently observed in the TVC, resulting in enormous pressure variations and hence a high level of noise [23]. The emitted noise in the model scale is typically visible in the spectrum as a hump in the mid-frequency region (200 to 800 Hz) and a broadband monopole-type cavitation noise contribution due to the dynamics, such as the bursting and rebounding of cavitation bubbles. In order to accurately simulate the TVC in CFD simulations, adaptive mesh refinement (AMR) techniques are utilised to improve URN predictions, e.g. [13,24]. However, to capture the time-dependent dynamics of the TVC, a dynamic adaptive mesh refinement technique is better suited for such high-fidelity simulations. The impact of TVC modelling on the noise spectrum has been assessed within the scope of the current study using this approach.

Within the above framework, the present study presents a numerical investigation of a marine propeller's noise prediction compared with the available experimental URN database based on the King's College-D. Because of the significant variation in cavitation types and the resulting variations in the URN spectral response, the particular member of the series (KCD-193) was chosen for the comparison [25,26]. In order to understand the influence of various simulation aspects on prediction accuracy, the experimental results were compared with the numerical predictions of URN under different flow conditions, represented by varying advance coefficients and cavitation numbers. For an accurate URN prediction, the occurrence of TVC was identified as a critical factor that numerical simulations must capture well. Since the effect of TVC on the noise spectrum is claimed to be significant, including its emergence and sustained presence dominating the frequency response of the broadband hump [25], a systematic and dynamic adaptive mesh refinement strategy is required to develop solving the TV flow characteristics in the propeller slipstream and improve its prediction accuracy. The sensitivity of the broadband hump on the URN spectrum is also linked to the phenomenon of cavitation

bubble growth and collapse cycle. It will be most interesting to explore how the broadband hump's central frequency would vary with the propeller's loading condition represented by the advance coefficient and cavitation number. It is reported that the URN levels of a propeller at a higher frequency region can be reduced slightly with increasing propeller loading (i.e. reduced advance coefficient and developing cavitation), resulting in a cushioning effect on the spectrum [27]. It is also claimed that the tip-vortex cavitation resolution is directly related to the accurate assessment of the noise spectrum, particularly around the broadband hump frequency bandwidth. Therefore, this study aims to predict the URN spectra of marine propellers more accurately. In order to achieve the aim, the study objectives are specified as: (i) to capture the tip vortex cavitation characteristics of the flow by introducing a dynamic adaptive mesh refinement technique; and (ii) to understand the contributions of the nonlinear noise sources, i.e., the vorticity and turbulence characteristics of the flow, under non-cavitating and cavitating conditions.

In order to present the study results, the paper is arranged as: by following this introductory section; the details of the experimental study, testing facility, procedures and test cases are presented in Section 2. This is followed by the details of the numerical modelling, including the computational domain, grid topology, and analytical features in Section 3. The results and discussions of the study are presented in Section 4, followed by the concluding remarks in Section 5.

2. Experimental study

The experimental studies were carried out in two stages at the Emerson Cavitation Tunnel (ECT) of Newcastle University (NCL), which has a rectangular test section with a cross-section of 1.22 $m \times$ 0.81 m *(BxH)*. The propeller model utilised for these tests was the Meridian Series KCD 193, having a 304.80 mm diameter (*D*) with a design pitch (*P*) ratio of $P_{0.7}/D = 1.00$ (Fig. 1) and two groups of tests were conducted with this model. The first group tests consisted of measuring the thrust (*T*) and torque (*Q*) to obtain the propeller open-water characteristics. The second group tests comprised the cavitation observations and noise measurements. The open-water experiments should be performed at a Reynolds (*Re*) number greater than 2×10^5 to minimise the scale effect, according to the ITTC procedure [28]. However, recognizing that $Re = 2 \times 10^5$ may not be sufficient, the scale effect could be addressed through a comprehensive test campaign involving varying sizes of model propellers. Consequently, the experiments were performed in a range of $Re = 1 \times 10^6$ to 1.5×10^6, assumed to be sufficient for this study. Furthermore, the measurements were repeated at least five times to ensure a satisfactory level of uncertainty, following the proposed guidelines by ITTC [29]. All the cavitation observations and noise measurements were conducted in the open-water condition at a 3.00 ms^{-1} tunnel inflow speed (*V*) recorded at the tunnel's test section under three different vacuum circumstances.

2.1. Model test procedure

The experiments were carried out using the ECT's Kempf & Remmers H33-type dynamometer. According to the model test procedure, the propeller is replaced by a dummy hub of the same mass and diameter of the propeller to eliminate the effects of friction. The thrust and torque measurements were corrected, considering the boss drag and idle torque calibration curve. The cavitation observations were recorded with a high-speed video camera (2000 fps), supported by a synchronised stroboscope and a continuous light source. The corresponding cavitation number (σ_n) was determined based on the ambient pressure, p_0, of the cavitation tunnel, and the rotational speed of the propeller (*n*) as in Eq. (1). A barometer was used to measure the ambient pressure (i.e., atmospheric pressure) in the laboratory.

$$\sigma_n = \frac{p_0 - p_v + \rho g h_s}{0.5\rho(ND)^2} \tag{1}$$

where p_v is the vapour pressure, ρ is the density of water, g is the acceleration due to gravity, and h_s is the shaft immersion. The cavitation observations should be conducted under certain water quality conditions [30]. The water quality of the ECT is observed throughout the tests by a dedicated water quality monitoring system and degassing system to keep the oxygen saturation level of the cavitation tunnel at the desired level, as it significantly impacts the measurements.

The noise measurements were carried out using a Bruel & Kjaer miniature type 8103 hydrophone mounted within the cavitation tunnel in a streamlined strut. The hydrophone was located facing the flow and at a location in the tunnel, whose offset is given in
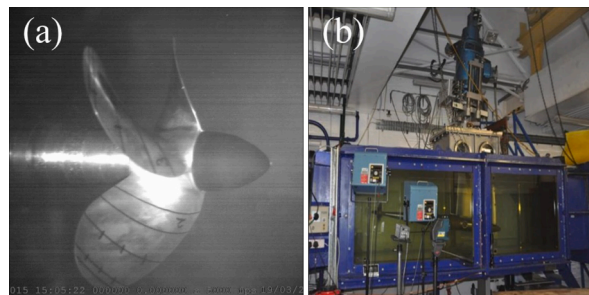

Fig. 1. (a) Meridian Series KCD 193 Propeller, (b) Experimental configuration of cavitation observation and noise measurement.

Table 1, relative to the acoustic centre (model propeller shaft axis).

The URN levels *(L)* were recorded by a digital acquisition and analysis software (PULSE) system. The acquired data was corrected to the standard measuring distance of a one-meter source level using the spherical acoustic wave propagation expression as

$$L_s = L_p + 20\log_{10}(d\,/\,d_{ref}) \tag{2}$$

where L_s is the URN level at 1 m, L_p sound pressure level (SPL), d is the resultant distance hydrophone to the acoustic centre, and d_{ref} is the distance of 1 m. The following equation is used to correct (L_p') the measured noise considering the cavitation tunnel background noise [31].

$$L_p' = 10\log_{10}\left[10^{(L_{p_{s+n}}/10)} - 10^{(L_{p_n}/10)}\right] \tag{3}$$

where $L_{p_{s+n}}$ is the SPL of the noise measurement, and L_{p_n} is the SPL of the associated background noise measurement. The background noise measurements of the cavitation tunnel are made using a dummy hub in the place of the propeller, and correction is applied depending on the level of the differences in measurements following the American National Standard Institute (ANSI) procedure [32]. The cavitation tunnels are closed-cycle circulation channels. The noise measurements suffer from reverberations due to the reflected waves and boundary motions. In order to acquire the acoustic transfer functions of the ECT, a calibrated noise source was attached to the propeller plane and connected to an arbitrary waveform generator, which produced sinusoidal sweep signals. The ECT's reverberation characteristics were observed to be remarkably similar to the other experimental facilities [33]. The results of the reverberation study are not involved as a correction to the noise measurements due to the limited frequency range that the signal-to-noise ratio of the measurements would be reliable. Therefore, the results given in the current study on the comparison of the measurements and the numerical noise predictions are not a validation study because the measured noise signal may be affected by the confined space made up of the cavitation tunnel and the placement of the hydrophone; instead, the comparisons are to assess the response of the numerical analyses on the effect of the accurate vortex modelling to the noise predictions, referring to the measurements. Further details of the model test procedure on cavitation observation and noise measurement were provided in Aktas [25].

2.2. Test cases

The characteristics of the KCD 193 model propeller and the conditions for the test cases are given in Table 2, where *Z* is the number of blades, A_E propeller expanded blade area, A_0 propeller disc area, *T* water temperature during the tests, ν kinematic viscosity and *DO* is the dissolved oxygen content of the cavitation tunnel measured during the experiments as recommended by ITTC procedure [30].

The test matrix to be addressed on cavitation observations and noise measurements for various advance coefficients, $J = V \times (N\,D)^{-1}$, and cavitation numbers are presented in Table 3, where p^- denotes the level of applied vacuum set before each test.

3. Numerical study

The numerical studies based on the Computational Fluid Dynamics (CFD) method were performed in two stages using the ANSYS (18.2) Fluent commercial software. The level of the numerical uncertainty was quantified in terms of the dependency analysis. Once the grid and time step size were determined, cavitation modelling and noise prediction simulations were conducted. The open-water simulations to compare the thrust (K_T) and torque (K_Q) coefficients and open water (η_0) efficiency of the model propeller by the experimental results were carried out by following the ITTC procedure [28]. A Dynamic Adaptive Mesh Refinement approach was developed to model the tip vortex cavitation characteristics. An interior permeable surface that encloses the propeller and partially the up and downstream of the propeller was generated to define the acoustic source for the application of the acoustic analogy. In this way, the contribution of the nonlinear noise sources, represented by turbulence and vorticity, is included in the noise predictions.

3.1. Methodology

The incompressible Scale-Adaptive Simulation (SAS) model was utilised in the numerical analyses with the SST (Shear Stress Transport) k-ω turbulence model based on the Boussinesq hypothesis [34]. A segregated algorithm was used in conjunction with the finite-volume method [35] to solve the momentum and turbulent transport equations. The pressure-correction-based SIMPLE technique [36] was used to couple the pressure and velocity fields. The spatial discretisation of the convective terms of the Navier-Stokes and turbulent transport equations was acquired with a second-order-upwind scheme [37], whilst a bounded central differencing

Table 1
Offset of hydrophone (8103) location to acoustic centre in the experiments.

Coordinate	Distance (m)
X	0.264
Y	0.245
Z	0.120

Table 2

The characteristics of the KCD 193 propeller and the conditions for the test case.

Parameter	Value	Unit
Z	4	–
BAR (A_E/A_0)	0.65	–
T	1 4.80	°C
ρ	999.13	kg m^{-3}
ν	1.14×10^{-6}	m^2 s^{-1}
DO	30	%

Table 3

The test matrix for various advance coefficients and cavitation numbers ($V = 3.00$ ms^{-1}).

N (1/s)	p^- (kPa)	J	σ
16.67	Atm.	0.59	0.87
20.00	Atm.	0.49	0.60
23.33	Atm.	0.42	0.45
25.00	Atm.	0.39	0.39
16.67	20	0.59	0.72
20.00	20	0.49	0.50
23.33	20	0.42	0.37
25.00	20	0.39	0.32
13.33	40	0.74	0.86
16.67	40	0.59	0.57
20.00	40	0.49	0.39
23.33	40	0.42	0.30
25.00	40	0.39	0.26

scheme was used for the viscous terms. The divergence of the mixture velocity is zero for the incompressible flow. However, in the cavitating flow, cavity evaporation and condensation cause a volume dilation, and the divergence of the mixture velocity does not vanish. Therefore, the general form of the conservation equations, valid for incompressible and compressible flows, is expressed in Cartesian tensor notation as follows.

$$\frac{\partial \rho}{\partial t} + \frac{\partial (\rho u_i)}{\partial x_i} = 0 \tag{4}$$

$$\frac{\partial (\rho u_i)}{\partial t} + \frac{\partial (\rho u_i u_j)}{\partial x_j} = -\frac{\partial p}{\partial x_i} + \frac{\partial}{\partial x_j}\left[\mu\left(\frac{\partial u_i}{\partial x_j} + \frac{\partial u_j}{\partial x_i} - \frac{2}{3}\delta_{ij}\frac{\partial u_l}{\partial x_l}\right)\right] + \frac{\partial\left(-\overline{\rho u_i' u_j'}\right)}{\partial x_j} \tag{5}$$

where ρ is the liquid density, u averaged velocity, p averaged static pressure, u$^{'}$ fluctuating velocity and δ_{ij} is the Kronecker delta. $\overline{\rho u_i' u_j'}$ denotes the Reynolds stress term produced by turbulent fluctuations, and the overbar represents a short-hand average. The Boussinesq hypothesis relates the Reynolds stresses to the mean velocity gradients.

$$-\overline{\rho u_i' u_j'} = \mu_t\left(\frac{\partial u_i}{\partial x_j} + \frac{\partial u_j}{\partial x_i}\right) - \frac{2}{3}\left(\rho k + \mu_t\frac{\partial u_k}{\partial x_k}\right)\delta_{ij} \tag{6}$$

where μ_t and k denote the turbulent viscosity and turbulent kinetic energy, respectively. The SST-SAS model is an advanced unsteady RANS (URANS) model that can produce spectral content for unstable flows [38] and may provide solutions with LES-like behaviour. The transport equations for the SST-SAS model are based on transforming Rotta's approach to k-ω (SST) and are defined as follows.

$$\frac{\partial \rho k}{\partial t} + \frac{\partial (\rho u_i k)}{\partial x_i} = G_k - \rho c_\mu k\omega + \frac{\partial}{\partial x_j}\left[\left(\mu + \frac{\mu_t}{\sigma_k}\right)\frac{\partial k}{\partial x_j}\right] \tag{7}$$

$$\frac{\partial \rho \omega}{\partial t} + \frac{\partial (\rho u_i \omega)}{\partial x_i} = \alpha\frac{\omega}{k}G_k - \rho\beta\omega^2 + Q_{SAS} + \frac{\partial}{\partial x_i}\left[\left(\mu + \frac{\mu_t}{\sigma_\omega}\right)\frac{\partial \omega}{\partial x_j}\right] + (1-F_1)\frac{2\rho}{\sigma_{\omega,2}}\frac{1}{\omega}\frac{\partial k}{\partial x_j}\frac{\partial \omega}{\partial x_j} \tag{8}$$

where G_k is the production of turbulent kinetic energy and $\sigma_{\omega,2}$ is the σ_ω value for the k-ε regime of the SST model. F_1 denotes a function to be used for blending the ω Eq. (7) with the ε Eq. (8). The SST-SAS model varies from the SST-RANS model by an additional source term, Q_{SAS}, in the transport equation for the turbulence eddy frequency (ω). This additional term originates from a second-order derivative term in Rotta's transport equation and is expressed as follows.

$$Q_{SAS} = \max\left[\rho\eta_2\kappa S^2\left(\frac{L}{L_{vK}}\right)^2 - C\frac{2\rho k}{\sigma_f}\max\left(\frac{1}{\omega^2}\frac{\partial\omega}{\partial x_j}\frac{\partial\omega}{\partial x_j}, \frac{1}{k^2}\frac{\partial k}{\partial x_j}\frac{\partial k}{\partial x_j}\right), 0\right] \tag{9}$$

where the model parameters are $\eta_2 = 3.51$, $\sigma_\phi = 2/3$, $C_{SAS} = 2.0$, and $L = \sqrt{k}/(c_\mu^{1/4}\omega)$ is the length scale of the modelled turbulence. The von Karman length scale in Eq. (10), L_{vK}, is used as a trigger in detecting unstable flows, enabling the SST-SAS model to be simultaneously scale-adaptive to the resolved eddy structures in the URANS computations [39].

$$L_{vK} = \kappa\frac{\partial u}{\partial y}\bigg/\frac{\partial^2 u}{\partial y^2} \tag{10}$$

where $\kappa = 0.41$ is the von Karman constant, and the first velocity derivative represented in Eq. (10) is equal to $\partial u/\partial y = S = \sqrt{2S_{ij}S_{ij}}$, a scalar invariant of the strain rate tensor $S_{ij} = 1/2(\partial u_i/\partial x_j + \partial u_j/\partial x_i)$. The second velocity derivative in Eq. (10) is generalised to three-dimensional using the magnitude of the velocity Laplacian $\partial^2 u/\partial y^2 = [(\partial^2 u_i/\partial^2 x_k^2)/(\partial^2 u_i/\partial^2 x_j^2)]^{1/2}$. A further detailed account of the SST-SAS model can be found in Ref. [38].

The mixture model theory is used to model multiphase flows, where the phases move at different velocities but assume local equilibrium over short spatial length scales. The mixture model solves the mixture momentum equation and prescribes relative velocities to describe the dispersed phases. The mixture model assumes that both phases (liquid and vapour) are homogenous. The continuity and momentum equations for the mixture are as follows.

$$\frac{\partial}{\partial t}(\rho_m) + \nabla\cdot\left(\rho_m\overrightarrow{v}_m\right) = 0 \tag{11}$$

$$\frac{\partial}{\partial t}\left(\rho_m\overrightarrow{v}_m\right) + \nabla\cdot\left(\rho_m\overrightarrow{v}_m\overrightarrow{v}_m\right) = -\nabla p + \nabla\cdot\left[\mu_m\left(\nabla\overrightarrow{v}_m + \overrightarrow{v}_m^T\right)\right] + \rho_m\overrightarrow{g} + \overrightarrow{F} \tag{12}$$

where $\rho_m = \alpha_v\rho_v + (1-\alpha_v)\rho_l$ is the density of the mixture, $\overrightarrow{v}_m$ mass-averaged velocity, $\overrightarrow{F}$ body force, $\mu_m = \alpha_v\mu_v + (1-\alpha_v)\mu_l$ the viscosity of the mixture and α_v is the volume fraction of vapour. The multiphase mass transfer (evaporation and condensation) is governed by the vapour transport equation as

$$\frac{\partial}{\partial t}(\alpha_v\rho_v) + \nabla\cdot\left(\alpha_v\rho_v\overrightarrow{v}_m\right) = R_e - R_c \tag{13}$$

The mass transfer source terms R_e and R_c in Eqs. (14) and (15) are connected to the growth and collapse of the vapour bubbles, respectively. The volume fraction of vapour was solved by Schnerr and Sauer's model [40], implementing a simplified Rayleigh-Plesset [41] equation, which ignores the impact of bubble growth acceleration, viscous effects, and surface tension force.

$$R_e = \frac{\rho_v\rho_l}{\rho_m}\alpha_v(1-\alpha_v)\frac{3}{R_B}\sqrt{\frac{2}{3}\frac{p_v-p}{\rho_l}} \tag{14}$$

$$R_c = \frac{\rho_v\rho_l}{\rho_m}\alpha_v(1-\alpha_v)\frac{3}{R_B}\sqrt{\frac{2}{3}\frac{p-p_v}{\rho_l}} \tag{15}$$

where p_v is the vapour pressure and R_B is the bubble radius given by Eq. (16), where n_0 is the bubble number density and was set as the 5×10^7 m^{-3} by an approximation of the experimental value of air content measurements conducted during the tests.

$$R_B = \left(\frac{\alpha_v}{1-\alpha_v}\frac{3}{4\pi}\frac{1}{n_0}\right)^{1/3} \tag{16}$$

$$\frac{dR_B}{dt} = \sqrt{\frac{2}{3}\frac{p_b-p}{\rho_l}} \tag{17}$$

In Eq. (17), the simplified Rayleigh-Plesset equation was used, neglecting the second-order terms and the surface tension force regarding the high level of the pressure difference (p_b-p), where p_b is the bubble surface pressure.

The noise predictions were performed, incorporating convective effects, by the permeable form of the Ffowcs-Williams and Hawkings acoustic analogy as an inhomogeneous wave equation that can be derived by manipulating the continuity equation and the Navier-Stokes equation. The FW-H equation is given in Eq. (18) following [8,42].

$$\frac{1}{a_0^2}\frac{\partial^2 p'}{\partial t^2} - \nabla^2 p' = \frac{\partial^2}{\partial x_i\partial x_j}\left[T_{ij}H(f)\right] - \frac{\partial}{\partial x_i}\left\{\left[P_{ij}n_j + \rho u_i(u_n - v_n)\right]\delta(f)\right\}$$
$$+ \frac{\partial}{\partial t}\left\{\left[\rho_0 v_n + \rho(u_n - v_n)\right]\delta(f)\right\} \tag{18}$$

where $p' = p - p_0$ is the sound pressure at the far field, subscript n denotes the velocity component normal to the surface, $\delta(f)$ Dirac delta function, $H(f)$ Heaviside function, $T_{ij} = \rho u_i u_j + P_{ij} - a_0^2 \rho' \delta_{ij}$ Lighthill stress tensor, and $P_{ij} = p\delta_{ij} - \mu[\partial u_i / \partial x_j + \partial u_j / \partial x_i - (2/3)(\partial u_k / \partial x_k)\delta_{ij}]$ is the compressive stress tensor. The solution of Eq. (18) consists of surface and volume integrals. The surface integrals represent the monopole $(\partial / \partial t\{[\rho_0 v_n + \rho(u_n - v_n)]\delta(f)\})$ and dipole $(\partial / \partial x_i\{[P_{ij}n_j + \rho u_i(u_n - v_n)]\delta(f)\})$ acoustic sources and partially quadrupole sources. The volume integrals represent the quadrupole $(\partial^2 / \partial x_i \partial x_j [T_{ij}H(f)])$ sources. In accordance with the permeable formulation adopted for the acoustic analogy used in the simulations, the first term on the right side of Eq. (18) is dropped due to the negligible contributions of the volume integrals in Eq. (19).

$$p'(\overrightarrow{x}, t) = p'_T(\overrightarrow{x}, t) + p'_L(\overrightarrow{x}, t) \tag{19}$$

where $p'_T(\overrightarrow{x}, t)$ is the thickness term (Eq. (20)), and $p'_L(\overrightarrow{x}, t)$ is the loading term (Eq. (21)).

$$4\pi p'_T(\overrightarrow{x}, t) = \int_{f=0} \left[\frac{\rho_0(\dot{U}_n + U_{\dot{n}})}{r(1 - M_r)^2}\right] dS + \int_{f=0} \left[\frac{\rho_0 U_n \{r\dot{M}_r + c(M_r - M^2)\}}{r^2(1 - M_r)^3}\right] d \tag{20}$$

$$4\pi p'_L(\overrightarrow{x}, t) = \frac{1}{c} \int_{f=0} \left[\frac{\dot{L}_r}{r(1 - M_r)^2}\right] dS + \int_{f=0} \left[\frac{L_r - L_M}{r^2(1 - M_r)^2}\right] dS$$
$$+ \int_{f=0} \left[\frac{L_r\{r\dot{M}_r + c(M_r - M^2)\}}{r^2(1 - M_r)^3}\right] dS \tag{21}$$

The square brackets in Eqs. (20) and (21) denote that the kernels of the integrals are computed at the corresponding retarded times, $\tau = t - r/a_0$, where t is the observer time and r is the distance to the observer. The subscripted quantities, as the inner products of a vector and a unit vector implied by the subscript, are $L_r = \overrightarrow{L} \cdot \overrightarrow{r} = L_i r_i$ and $U_r = \overrightarrow{L} \cdot \overrightarrow{r} = L_i r_i$ where $\overrightarrow{r}$ and $\overrightarrow{n}$ denote the unit vectors in the radiation and wall-normal directions, respectively. In the noise predictions, an interior permeable surface was defined as an acoustic source. Hence, the quadrupole sources within the region enclosed by the source surface are included in Eqs. (20) and (21).

In computational studies, verification and validation analyses are required to determine the level of numerical uncertainty. The simulation error ($\delta_S = S-T = \delta_{SM} + \delta_{SN}$) is to be found considering the result of the analysis (S) and the actual value (T), comprising the modelling (δ_{SM}) and numerical errors (δ_{SN}). The numerical uncertainty (U_{SN}), as a verification of the simulations, consists of solver and solution verifications. As the principal concern is to focus on the verification of the solution, ignoring the contributions of solver verification, round-off error, and the numerical error for the iteration number (δ_I) and other parameters (δ_P), the numerical uncertainty is expressed as follows.

$$U_{SN} = \sqrt{U_G^2 + U_T^2} \tag{22}$$

In Eq. (22), U_G and U_T are grid and time step components of the numerical uncertainty, respectively. The Least Squares Root (LSR) method [43] was used to obtain the level of the numerical uncertainty. The LSR method based on Richardson Extrapolation (RE) considers the scatter of numerical solutions and requires at least four grid densities due to, typically in complex flows, grids leading to variability.

$$\delta_{RE} = S_i - S_0 = \alpha h_i^q \tag{23}$$

In Eq. (23), δ_{RE} is the discretisation error, S_i is the solution obtained by the simulations, S_0 is the extrapolated solution, α is a constant, h_i grid refinement ratio, and q is the observed order of accuracy. Those, S_0 and α, are to be found performing a curve fit of Eq. (23) using the scatter of numerical solutions. The observed order of accuracy refers to the monotonic convergence ($q > 0$) or divergence ($q < 0$) and is used to estimate the error depending on the scatter. The error estimate is based on the general RE form in Eq. (23) and a further alternative method depending on the scatter. In a range of *$0.5 \leq q \leq 2$* and *$q > 2$*, Eqs. (23) and (24) are used, respectively, whilst the best fit of Eqs. (24) and (25) is utilised for the *$q < 0.5$*. If there is an oscillatory or anomalous convergence, which is defined as being when the solution is alternately above and below the exact solution, the uncertainty is based on the data range parameter (δ_{Δ_M}) as given in Eq. (26).

$$\delta_{RE}^{02} = S_i - S_0 = \alpha_{02} h_i^2 \tag{24}$$

$$\delta_{RE}^{12} = S_i - S_0 = \alpha_{11} h_i + \alpha_{12} h_i^2 \tag{25}$$

$$\delta_{\Delta_M} = \left[(S_i)_{max} - (S_i)_{min}\right] / \left[(h_n / h_1) - 1\right] \tag{26}$$

A factor of safety (F_S) is applied, 1.25 in a range of *$0.5 \leq q \leq 2$*, to the discretisation error (δ_{RE}) to evaluate the numerical uncertainty. In contrast, F_S is considered as 3 by the out of the given range. In order to assess if validation is achieved, the comparison error ($E=D-S$) is associated with validation uncertainty (U_V), as given in Eq. (27), where $E < U_V$ refers to validation achieved at the U_V

level.

$$U_V = \sqrt{U_D^2 + U_{SN}^2}$$

(27)

where U_D denotes the uncertainty of the experiments and *D* is the data.

3.2. Computational domain and mesh topology

The computational domain(s) size to be used in the simulations were determined following the ITTC procedure [44] and cross-section (1.22 *m* × 0.81 m) of the Emerson Cavitation Tunnel test section, respectively. The aim of using two computational domains, one larger domain (Fig. 2a) and the latter the same domain as the experiments having hard-wall boundary conditions (Fig. 2b), is to quantify the effect of the cavitation tunnel test section alone, ignoring the contraction and diffuser sections. In Fig. 2(a) and (b), velocity inlet and pressure outlet conditions were defined for the boundaries' *(-) x* direction and *(+) x* direction, respectively. The symmetry condition was defined for the shaft (yellow-coloured) and the circular region between the velocity inlet and pressure outlet boundaries in Fig. 2(a). The symmetry and no-slip wall conditions were defined for the shaft and the rectangular region between the velocity inlet and pressure outlet boundaries, respectively, in Fig. 2(b), whilst the no-slip wall condition was specified for the propeller, shaft, hub and hub cap in Fig. 2(c). The interface boundary condition was defined for the rest of the regions (i.e., blue-coloured acoustic source and red-coloured rotating regions in Fig. 2) within the computational domain to transfer the information from one cell zone to another. A number of receivers were defined in the computational domain to monitor and extract the pressure fluctuations, and the offset of receiver positions to propeller centre is given in Table 4.

A permeable surface (Fig. 2c) was defined as the acoustic source due to cavitation being a volume source term and to include the contribution of non-linear terms based on the instantaneous shear stress and vorticity content in a highly turbulent flow domain [47, 49]. The definition of the permeable surface requires further effort regarding its size (i.e., radial and axial distance by the acoustic source) and shape, which may affect noise levels, frequency content, and directionality if the integration of the incompressible simulation and FW-H acoustic analogy is the concern, as in the present study [46]. A directionality effect and, hence, discretisation
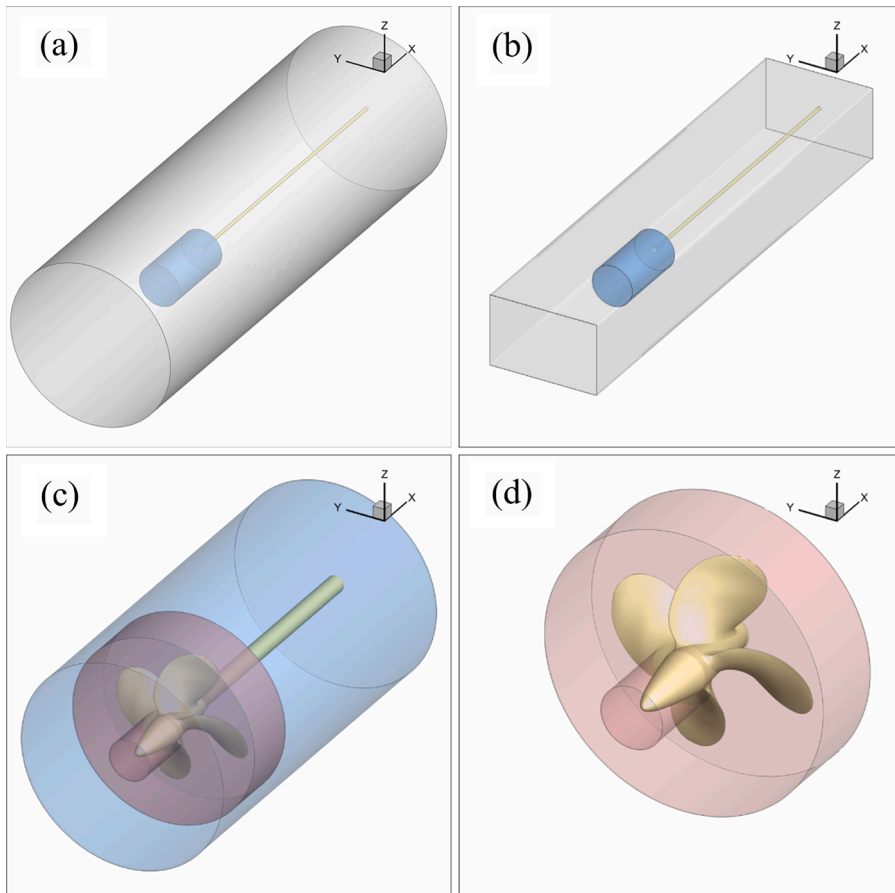

Fig. 2. The computational domains used in the simulations. (a) and (b) Static regions, (c) Acoustic source (blue-coloured) and Rotating region (red-coloured), (d) Rotating region.

Table 4

Offset of receiver positions to propeller centre in the simulations.

Rec.	X/D_P	Y/D_P	Z/D_P	Rec.	X/D_P	Y/D_P	Z/D_P	Rec.	X/D_P	Y/D_P	Z/D_P
01	0.50	0.00	0.35	**07**	0.00	0.00	1.18	**13**	1.17	0.00	0.00
02	0.00	0.00	0.56	**08**	0.00	0.96	0.00	**14**	0.58	1.01	0.00
03	0.00	0.00	0.62	**09**	0.00	1.17	0.00	**15**	0.58	1.01	0.00
04	0.00	0.00	0.71	**10**	0.00	1.38	0.00	**16**	1.38	0.00	0.00
05	0.00	0.00	0.89	**11**	0.00	1.58	0.00	**17**	0.69	1.19	0.00
06	0.00	0.00	1.04	**12**	0.00	1.79	0.00	**18**	0.69	1.19	0.00

errors and numerical dissipation may occur due to the distance of the acoustic source to the permeable surface, causing an erroneous prediction. The shape (e.g., spherical, cylindrical or rectangular prism) of the permeable surface may cause a deviation in a certain frequency level due to the flat end surfaces of the source [48]. Therefore, the size of the acoustic source, as an interior permeable surface, was determined considering the phase average of the vorticity (Ω) magnitude on the pre-defined circular sections and point receivers along the flow field within the steady-state condition (Fig. 3). The axial distance (X/D_P) among the sections is equal to $0.25 \times D_P$ and in a range of $[0 - 5] \times D_P$, whilst the vertical distance (Z/D_P) is varying between $[1.05 - 1.75] \times D_P$. The variation of the vorticity magnitudes on the consecutive circular sections and point sources are in a stable tendency following the $X/D_P = 2$, and $Z/D_P = 1.5$ positions, respectively, as shown in Fig. 3. Therefore, the length of the flow field (i.e., the acoustic source) was defined as $2 \times D_P$, and the diameter was chosen as $1.5 \times D_P$, conforming to the phase average trend of vorticity magnitudes.

An inner iteration (*i*)- terminate methodology was utilised depending upon the fluctuation of a variable (i.e. pressure fluctuation at
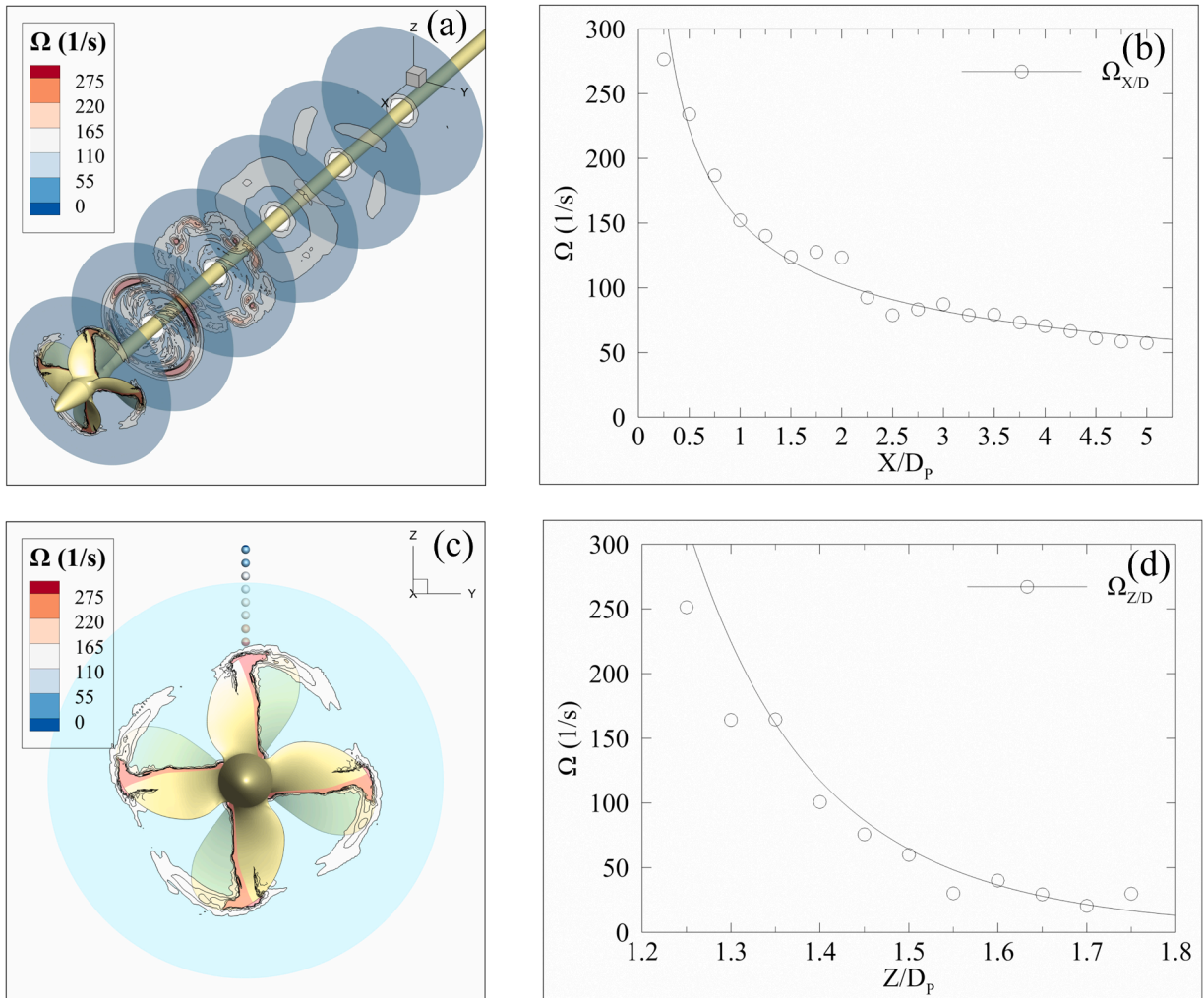
Fig. 3. Phase average of the vorticity (Ω) magnitude. (a) and (b) Circular sections ($X/D_P = 0, 1, 2, 3, 4, 5$) along the flow field, (c) and (d) point receivers along the Z direction (Z/D_P).

a nominated point in the downstream region); thus, once a pre-defined variation range criterion was satisfied, the related time step terminated (Fig. 4). In order to model the relative motion of the moving zone with respect to adjacent zones (i.e. static region), the Multiple Reference Frame (MRF) model was adopted at first to accelerate the convergence of the solution; then, the propeller's rotation was simulated by switching the relative motion to the Sliding Mesh (SM) model.

A systematic series of grid densities refined by a constant ratio, $\sqrt[4]{2}$, was used to quantify the numerical uncertainty through validation and verification analyses in open-water conditions. In addition, the time step dependency was scrutinised based on a constant value, *2*, considering the one-degree rotation rate of the propeller. A hybrid poly-hexacore (mosaic) mesh, derived by Fluent meshing, that conformally connects the octree hexes and layered poly-prism mesh with polyhedral elements (Fig. 6), was used to discretise the computational domain. The height of the first cell along the prism layer was defined in respect of the dimensionless wall distance, $y^+=1$, to resolve the boundary layer and the viscous sub-layer accurately.

The geometric definition of the propeller was constructed by dividing it into several parts, such as the tip *(0.95–1.00 r/R)*, the upper radii region *(0.70–0.95 r/R)*, leading edge (*LE*) and trailing edge (*TE*) parts of the upper radii region, the medium radii region *(0.30–0.70 r/R)*, *LE* and *TE* parts of the medium radii region, the lower radii *(0.20–0.30 r/R)* and hub *(0.00–0.20r/R)* regions (Fig. 5). The hub cap was divided into two parts along the *x* direction, the fore *(0.80–1.00 x/L)* and aft *(0.00–0.80 x/L)* parts. In the mesh topology, the dimensions of the cells were associated with the propeller's diameter and given in Table 5 regarding the fine grid.

In the cavitation analyses, the computational domain and the dimensions of the cells used in the open-water simulations were considered. However, the rotating region was extended in the *(-) x* direction to model the tip-vortex cavitation phenomenon precisely in accordance with the adaptive-mesh refinement approach (Fig. 6). The numerical results through cavitation analyses are to be used in the noise predictions. Therefore, the dimensions of the cells have been assigned equivalent, which means a uniform resolution was adopted inside the acoustic region, as shown in Fig. 6, excluding the propeller blades, hub and hub cap.

A dynamic adaptive-mesh refinement approach was implemented to model the tip-vortex cavitation phenomena as sketched in (Fig. 7). The isocontours of the vapour volume fraction field ($\alpha_v = 0.1$) caused by the cavitation were not included in the refinement region due to the fact that no further mesh refinement is required to model the cavitation. The downstream of the propeller was divided into several imaginary regions, considering the field (i.e. marked cells) length to be refined decreases in the *(-) x*-direction as the assigned variable increases. Thus, the magnitude of the variable is reduced as moving away from the source (i.e. propeller), and further refinement in the flow domain is avoided. The length of the imaginary regions is equal to $0.15 \times D_P$ and in a range of $[0–0.6] \times D_P$. The marked cells within each region along the downstream were adapted in four refinement levels, assigning an individual criterion on each level. A parent cell is subdivided into eight child cells on each refinement level. The adaptive-mesh refinement was implemented dynamically in a consecutive range (at a five-degree of propeller rotation rate). The refinement process was frozen temporarily once each refinement level was achieved to decrease the total number of cells to be refined and reinitiated following the numerical stability was ensured. As the cell size was refined through the simulations, the time step was decreased as well to confirm the numerical stability, depending on the Courant-Friedrichs-Levy criteria ($CFL \leq 1$). The Courant number is computed by dividing the product of flow velocity (*U*) and time step (Δt) by the cell size (Δx) as given in Eq. (28).

$$CFL = \left| \frac{U \Delta t}{\Delta x} \right| \leq 1 \tag{28}$$

In the noise spectra analysis, the appropriate cell sizes (Δ) were determined using Eq. (29). The solution of the initial steady-state simulation was used to obtain each cell size given in the square brackets in Eq. (29). The minimum of estimated cell sizes was defined to the acoustic region to be used in cavitation and noise analysis.

$$\min\left\{ \left[\Delta \leq \frac{\lambda}{20}, \lambda = \frac{c}{f_{\max}} \right], \left[\Delta = \frac{u'}{2F_{MC}}, u' = \sqrt{\frac{2}{3}k} \right], \left[\Delta \leq \frac{L}{2}, L = \sqrt{k} \Big/ \left(c_\mu^{1/4} \dot{\omega} \right) \right] \right\} \tag{29}$$

In Eq. (29), λ is the acoustic wavelength, c speed of sound ($c = 1500 \text{ ms}^{-1}$), $f_{\max}$ maximum frequency to be predicted, u' fluctuating velocity, F_{MC} cut-off frequency, k turbulent kinetic energy, L length scale of the modelled turbulence, c_μ a constant (0.09) and $\dot{\omega}$ is the turbulence eddy frequency.
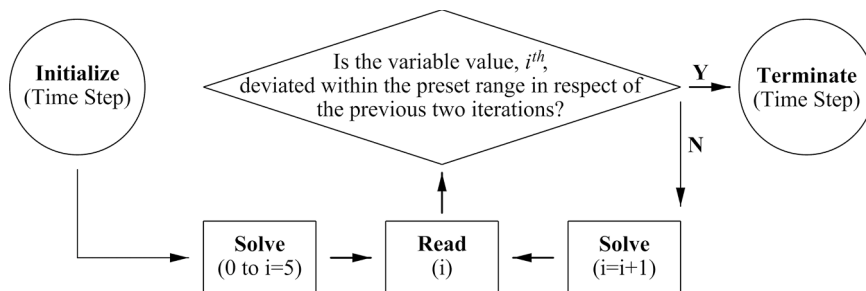

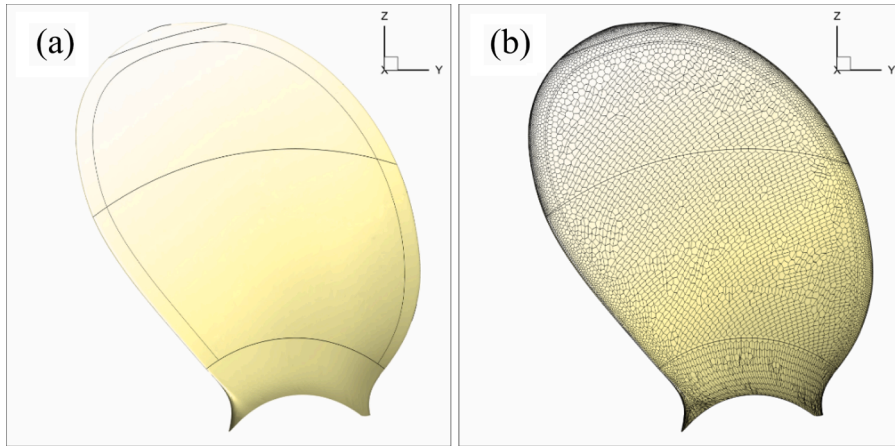**Fig. 4.** The inner iteration (*i*)-terminate methodology algorithm.

Fig. 5. The geometric definition (a) and surface mesh of the blade (b).

Table 5
The dimensions of the cells regarding the fine grid density.

Group	Position	Size
Tip	0.95–1.00 (r/R)	$(0.05D)/100$
Upper radii (UR)	0.70–0.95 (r/R)	$[(0.05D)/100, (0.50D)/100]$
$UR, LE \& TE$	0.70–0.95 (r/R)	$(0.05D)/100$
Med' radii (MR)	0.30–0.70 (r/R)	$[\sqrt[4]{2}(0.05D)/100, \sqrt[4]{2}(0.50D)/100]$
$MR, LE \& TE$	0.30–0.70 (r/R)	$\sqrt[4]{2}(0.05D)/100$
Lower radii	0.20–0.30 (r/R)	$\sqrt[4]{2}(0.50D)/100$
Hub	0.00–0.20 (r/R)	$\sqrt{2}(0.50D)/100$
Fore part	0.80–1.00 (x/L)	$\sqrt[4]{2}(0.05D)/100$
Back part	0.30–0.80 (x/L)	$\sqrt{2}(0.50D)/100$
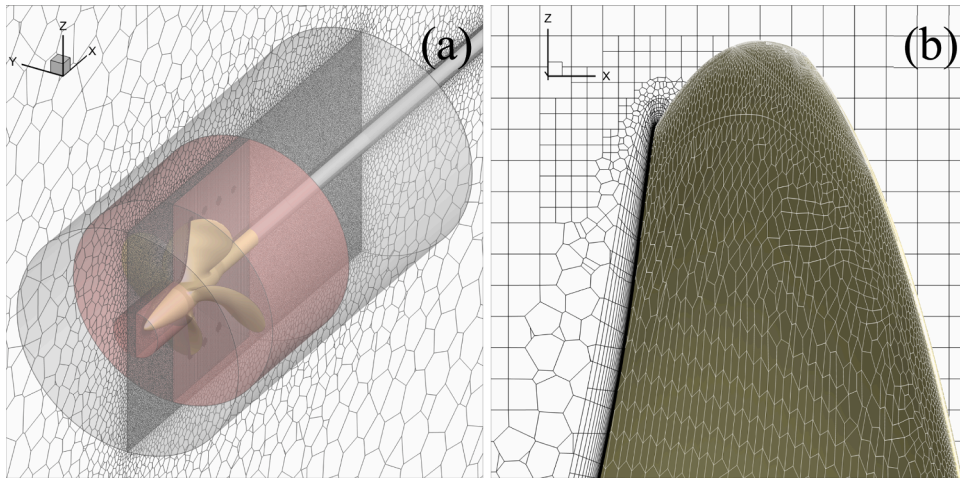
Fig. 6. The computational domain and poly-hexcore (mosaic) mesh used in the cavitation analyses and noise predictions.

4. Results and discussions

4.1. Experimental study

The open-water experiments were conducted by varying the tunnel inflow speed (V) and rotational rate of the propeller (n) so that the Reynolds (Re) number is greater than 2×10^5. The measurements were repeated at least five times, resulting in total uncertainty of the experiments (U_D) of 1.03 % for the thrust coefficient (K_T) and 2.53 % for the torque coefficient (K_Q). The uncertainty analysis

1ˢᵗ Stage Masking/excluding the iso-contours of the vapour volume fraction field is observed in the near field to the propeller.

2ⁿᵈ Stage Dividing the downstream of the propeller into imaginary regions and assigning individual criteria in these fields.

3ʳᵈ Stage Implementing the adaptive-mesh refinement dynamically in a consecutive range (five-degree of propeller rotation rate).

Fig. 7. Stages of the dynamic adaptive-mesh refinement approach.

method used follows that of the ANSI and American Society of Mechanical Engineers (ASME) standard on the measurement uncertainty, which is based on the root–sum–square (RSS) method. In addition, the effects of the advance coefficient (J) and cavitation number (σ_n) on the cavitation patterns and noise spectra were investigated based on the experimental results given in Table 3 and shown in Fig. 8 through 13.

The propeller-induced noise is affiliated with cavitation inception. The tip-vortex cavitation, typically the first form of propeller cavitation, results in high-pressure fluctuations and hence increased noise level. As shown in Fig. 8 through 10, the shape of the broadband hump and its peak frequency is initially dominated by the tip vortex cavitation rather than sheet cavitation with varying advance coefficients and cavitation numbers. In Fig. 8, the J is the same, and σ_n is varying; a broadband hump appears in the spectrum along with the cavitation inception ($J = 0.59$, $\sigma_n = 0.57$), a weak tip-vortex cavitation. A comparison of measured noise levels ($J = 0.49$) for the combinations of strong tip vortex cavitation with sheet cavitation ($\sigma_n = 0.39$), tip vortex cavitation with weak sheet cavitation ($\sigma_n = 0.50$) and weak tip-vortex cavitation alone ($\sigma_n = 0.60$) is given in Fig. 9. In the spectrum, the peak noise levels along the frequency range of the broadband hump(s), for $\sigma_n = 0.39$ in between 200 and 300 Hz, for $\sigma_n = 0.50$ in between 400 and 500 Hz and $\sigma_n = 0.60$ in between 600 and 700 Hz, are partially in agreement. In Fig. 10, J and σ_n vary based on the n; the J and σ_n decrease as the n increases, and the cavitation inception is in between $\sigma_n = 0.49$ and 0.59. The peak levels along the frequency range of the broadband hump(s) that appears with the cavitation inception agree; a combination of strong tip vortex cavitation with sheet cavitation for $\sigma_n = 0.42$ in between 200 and 300 Hz and the tip vortex cavitation alone for $\sigma_n = 0.49$ in between 600 and 700 Hz. An important excitation source of a vortex cavity is the shedding of vapour from the sheet cavity into the vortex cavity [26]. The extent of sheet cavitation and the strength of the vortex increases as the J and σ_n decrease, influencing the noise level and frequency range of the broadband hump and, in fact, the whole spectrum.

As observed in the experiments, since the frequency range of the broadband hump varied based on the advance coefficient (J) and cavitation number (σ_n), the broadband hump could not be associated with a specific frequency range. Instead, as the amount of cavitation increased, based on the reduced J number (Figs. 10, 11) and σ_n (Figs. 9, 12, 13), the central frequency of the broadband hump shifted towards the low-frequency range in the noise spectra with these two parameters. This trend is noteworthy to mention demonstrating the effect of local pressure variation on the cycle of the cavitation bubble (i.e. formation, growth and collapse), as consistently claimed in [45].

Based on the qualitative observations, one can claim that as the propeller loading increases, the cavitation extent (i.e. tip-vortex
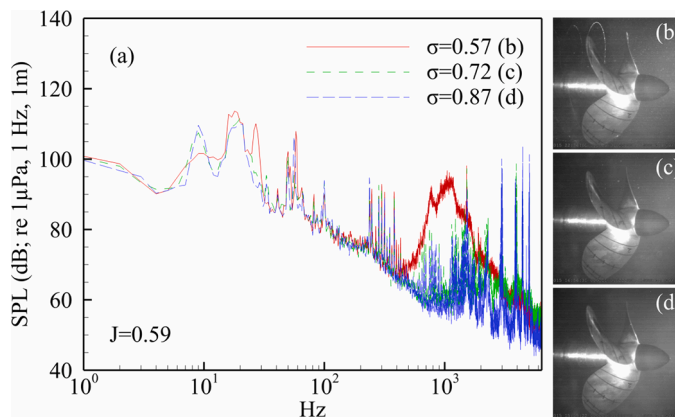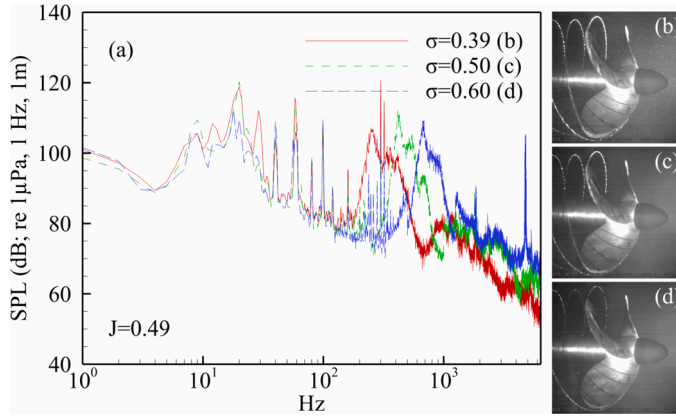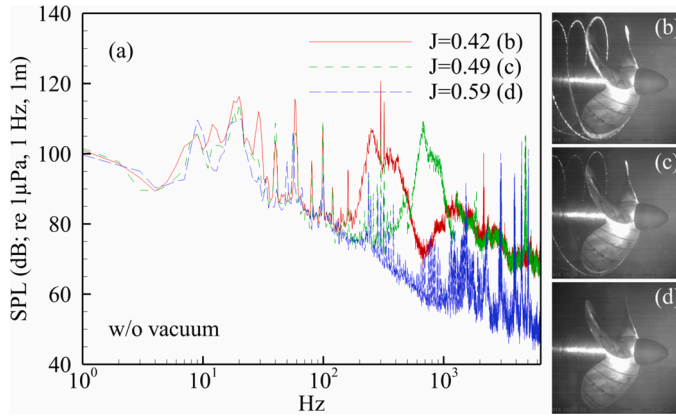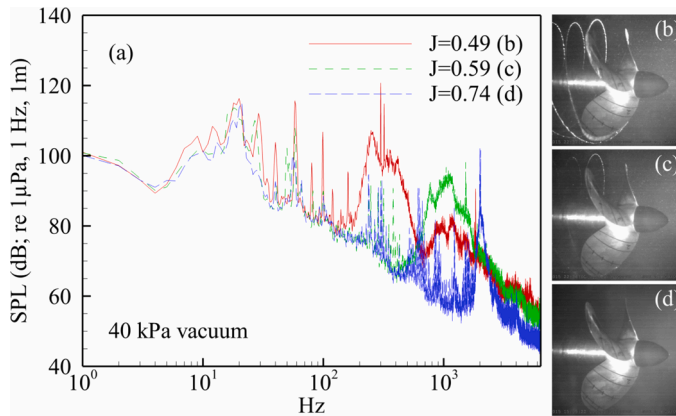

Fig. 8. Experimental results for the variable σ_n. (a) noise spectrum at constant $J = 0.59$; (b), (c), (d) view from top to bottom $\sigma_n = 0.57$, $\sigma_n = 0.72$ and $\sigma_n = 0.87$, respectively.

Fig. 9. Experimental results for the variable σ_n. (a) noise spectrum at constant $J = 0.49$; (b), (c), (d) view from top to bottom σ_n=0.39, σ_n=0.50 and σ_n=0.60, respectively.
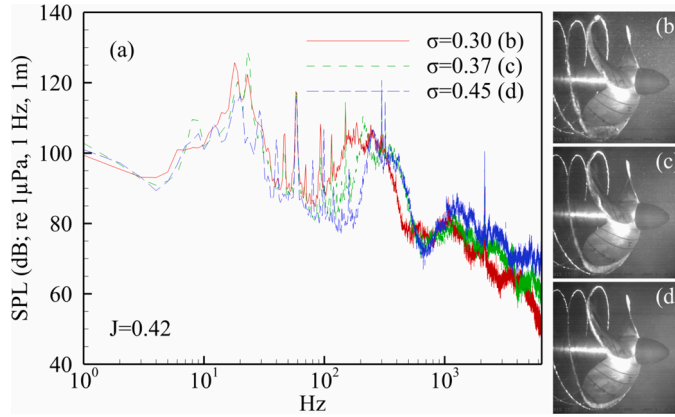

Fig. 10. Experimental results for the variable J. (a) noise spectrum at constant atmospheric ambient pressure; (b), (c), (d) view from top to bottom $J = 0.42$, $J = 0.49$ and $J = 0.59$, respectively.
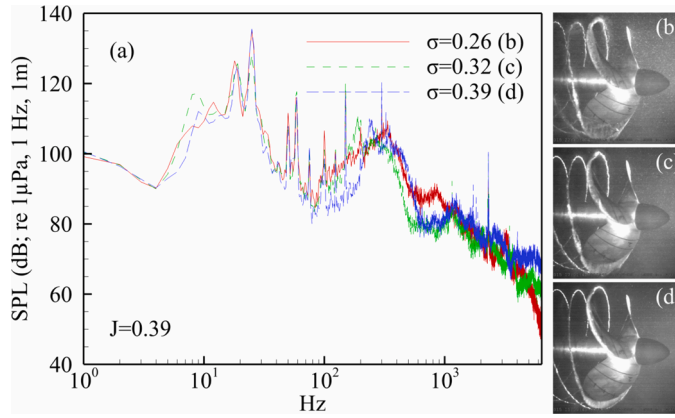

Fig. 11. Experimental results for the variable J. (a) noise spectrum at constant 40 kPa vacuum; (b), (c), (d) view from top to bottom $J = 0.49$, $J = 0.59$ and $J = 0.74$, respectively.

cavitation and sheet cavitation) also increases, hence the noise levels in the same manner (Figs. 8–13). In addition, the noise level in the high-frequency region was reduced slightly due to the extended cavitation (Figs. 12, 13), resulting in a cushioning effect of a cavitating bubble in the collapse stage in the spectrum.

Fig. 12. Experimental results for the variable σ_n. (a) noise spectrum at constant $J = 0.42$; (b), (c), (d) view from top to bottom $\sigma_n=0.30$, $\sigma_n=0.37$ and $\sigma_n=0.45$, respectively.

Fig. 13. Experimental results for the variable σ_n. (a) noise spectrum at constant $J = 0.39$; (b), (c), (d) view from top to bottom $\sigma_n=0.26$, $\sigma_n=0.32$ and $\sigma_n=0.39$, respectively.

4.2. Numerical study

The grid dependency analyses, at the advance coefficient of $J = 0.6$, were performed using four grids refined by $\sqrt[4]{2}$ in each axis direction, a systematic series of grid densities. In each grid density, the analyses were maintained until the average pressure at a nominated point in the downstream region over a single rotation of the propeller deviates less than 0.1 % relative to the previous one.

The average y^+ values along the wall and the total number of cells within various grid densities are given in Table 6. The amount of order of accuracy (q) and the numerical uncertainty (U_{SN}) derived by the grid and time dependency analyses are given in Table 7. The monotonic convergence, $q > 0$, was satisfied in terms of the accuracy level of the thrust (K_T) and torque (K_Q) coefficients.

In view of the uncertainty analyses, the results were validated in the level of the validation uncertainty (U_V) regarding the comparison error (E) based on the model tests, as given in Table 8.

As a result of the verification and validation analyses, the propeller open water coefficients were calculated via the fine grid density (*No 2*) and considering the one-degree rotation of the propeller on the definition of the physical time step and compared with the results of the model tests (Fig. 14).

As the propeller loading increases, the progress of the cavitation affects the propulsion performance adversely. The tip-vortex

Table 6
Average y^+ values and the total number of cells within the grids.

| No	Mesh Size	h_i/h_1	y^+
04	3.51×10^6	1.68	0.92
03	4.59×10^6	1.41	0.90
02	6.16×10^6	1.19	0.87
01	8.38×10^6	1.00	0.86

Table 7

Results of the grid and time dependency analyses.

	$U_{SN}\%S_{GD}$ (K_T)	$U_{SN}\%S_{GD}$ (K_Q)	$U_{SN}\%S_{TD}$ (K_T)	$U_{SN}\%S_{TD}$ (K_Q)
p	4.76	4.91	2.10	4.74
04	6.73	5.35	0.72	1.88
03	4.80	3.81	0.18	0.47
02	3.41	2.70	0.05	0.12
01	2.41	1.91	0.01	0.03

Table 8

Results of the uncertainty analyses.

No	$U_V\%D$ (K_T)	$U_V\%D$ (K_Q)	$E\%D$ (K_T)	$E\%D$ (K_Q)
04	6.74	6.12	1.48	1.71
03	4.80	4.52	2.30	2.35
02	3.47	3.65	2.73	2.74
01	2.86	3.14	2.82	2.79
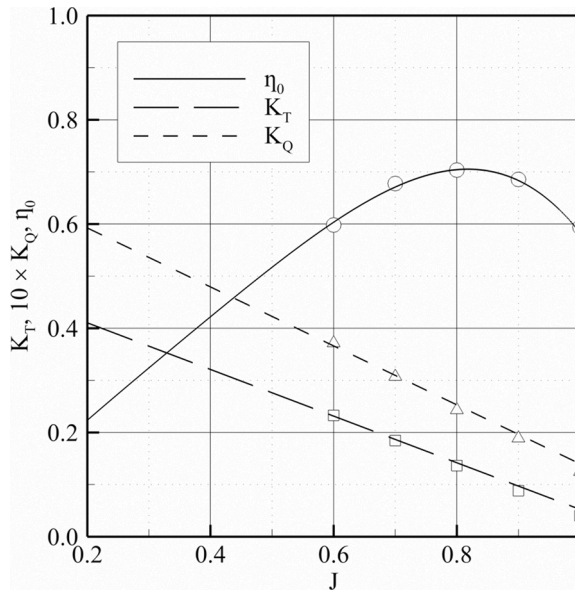
Fig. 14. Comparison of the experimental (lines) and numerical (symbols) propeller open-water coefficients.
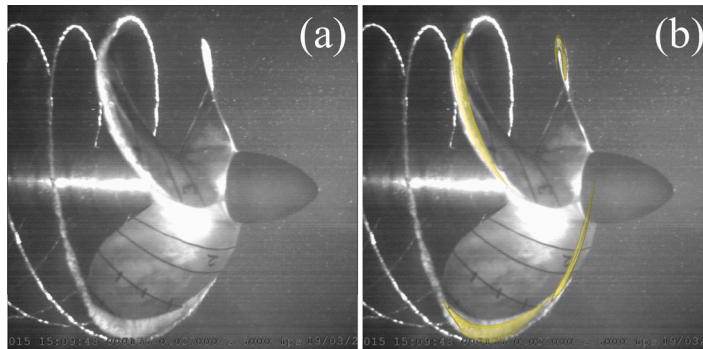
Fig. 15. Comparison of the cavitation patterns at $J = 0.39$ and $\sigma = 0.39$. (a) experimental, (b) experimental and numerical ($\alpha_v = 0.1$ %) results (yellow highlight indicates the prediction).

cavitation is typically the initial form of cavitation but contributes to and increases the level of underwater radiated noise significantly. In propeller design and hence numerical studies, an accurate prediction of this initial cavitation form is crucial. Therefore, the cavitation patterns derived via CFD analyses were compared with the experimental results. The analyses were performed with and without following a dynamic adaptive mesh refinement approach on the cavitation prediction ($J = 0.39$ and $\sigma = 0.39$) to demonstrate the effectiveness of the approach developed.

In the cavitation predictions, the physical time step was initially assigned considering the half-degree rotation of the propeller for each step. The volume fraction of vapour (α_v) was taken as 0.1 %, and the isocontours for the vapour phase was acquired and compared with the experiments as shown in Fig. 15.

The sheet cavitation began from the leading edge of the 0.5 *r/R* and expanded towards the tip region with a highly dynamic, cloudy tip vortex cavitation emanating from the propeller tip trailing edge area, as shown in Fig. 15. The sheet cavitation was observed to connect to a solid pre-existing tip-vortex, and to interact with it; an enduring vortex cavity was shed into the blade slipstream. A good agreement is shown when comparing cavitation development by the experiments with the predictions via analysis (yellow highlighted area in Fig. 15). On the other hand, the tip-vortex extent could not be predicted accurately due to insufficient mesh resolution in the TV trajectories.

In the numerical analyses, the extent of an isocontours within the computational domain can be extracted using several variables predefined in ANSYS Fluent software or defined by the end user. In respect of the adaptive mesh refinement approach, a variable to mark the cells to be adapted was determined regarding the response of the defined variable on the cavitation pattern and compared to the experiments. Initially, the volume fraction of vapour (α_v) was considered variable in a range of $\alpha_v = [0, 1]$. However, the initial grid size, specifically along the downstream, is insufficient to resolve the tip-vortex cavitation and could only provide an appropriate approach in the cavitating region. Then, regarding the effect of the local pressure distribution on the cavitation extent, the dynamic and absolute pressure variables were taken into account. The dynamic pressure, as a variable, could not mark the cells appropriately, whilst the refinement approach based on the absolute pressure was reasonable compared to the dynamic pressure. The cavitation phenomenon leads to distortion of the vorticity, typically rolling up into vortex tubes near the source. The Q-criterion, $Q > 0$, represents that the vorticity magnitude is prominent compared to the magnitude of the rate of strain (S) in the vortices areas and was found as the most appropriate variable to mark the cells. The refinement approach adapted the marked cells by the Q-criterion in a range of 2.5×10^5 to 20×10^5, as shown in Fig. 16.

The marked cells are subdivided into eight child cells on each refinement level; hence, the isotropic cell size, initially equal to 3.62 $\times 10^{-3}$ m in downstream, was reduced to 1.41×10^{-5} m at the end of the adaption stages. As a result of the four individual adaption stages, the total number of cells was obtained as 8.64×10^6, 9.31×10^6, 13.01×10^6 and 20.29×10^6, respectively. The last refinement level (i.e. fourth) is the critical stage regarding the variation of the total number of cells.

The tip-vortex cavitation, initially, could not be resolved even if the marked cells were adapted since the time step size was not manipulated. Therefore, as the cells were refined, Δt (Δt) was also decreased to confirm the numerical stability. In the last refinement level, the time step size was assigned as 1.39×10^{-5} s, approximately equal to the 0.125° rotation of the propeller.

Once the dynamic adaptive mesh refinement approach was completed, and the proper time step size was determined to resolve the tip-vortex cavitation, the vapour volume fraction was taken as 0.1 %, and the acquired cavitation pattern was compared well with the experiments, as shown in Fig. 17. In view of the comparison, the tip-vortex cavitation prediction highlighted by the yellow marker is in a good agreement with the experiments.

The noise predictions were performed in both configurations, without and with modelling the cavitation tunnel's test section, being the basis of further analysis to discuss the effect of the hard wall boundaries (tunnel walls) and the use of the FW-H in the near field. The
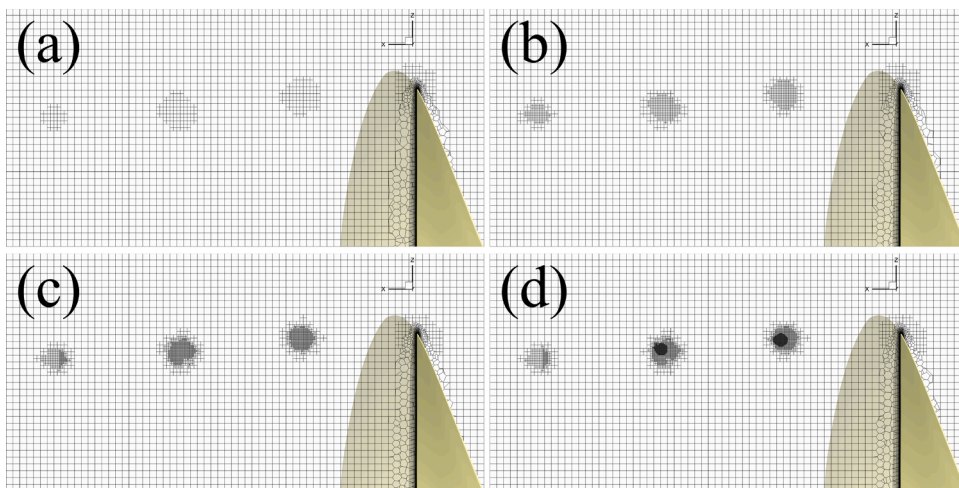
Fig. 16. Stages of the dynamic Adaptive Mesh Refinement approach. (a) first refinement level, (b) second refinement level, (c) third refinement level, (d) fourth refinement level.
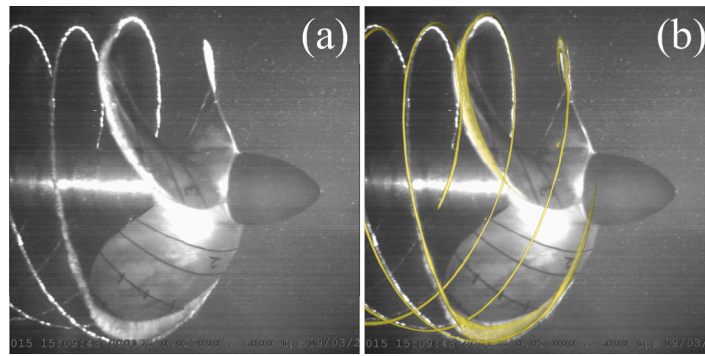
Fig. 17. Comparison of the experimental and numerical (adaptive mesh) cavitation patterns at $J = 0.39$ and $\sigma = 0.39$. (a) experimental, (b) experimental and numerical ($\alpha_v = 0.1$ %) results.

pressure fluctuations, extracted using the acoustic analogy (FW-H) and those directly provided by the SST-SAS model, were used to obtain sound pressure levels at the receivers at various radial and axial distances by the acoustic source (Fig. 18). The FW-H method applies only to predicting sound propagation toward free space, not to predicting the noise propagation inside ducts or a wall-enclosed domain. Initially, in the larger domain configuration, positions of the receivers were detected, and the sound levels were in good agreement with the FW-H method and direct noise calculation (DNC). The grid topology utilised in the cavitation analyses was not modified for the noise predictions. Instead, the noise predictions were initiated when the cavitation analyses converged. The frequency range to be considered through the analyses was determined regarding the assigned time step size and overall computational time. However, a certain level of the frequency range in spectra was assessed (Fig. 19) due to the broadband hump frequency level falling in a frequency range of [100, 1000] Hz regarding the experiments (Figs. 8–13). Furthermore, integrating the incompressible flow assumption and FW-H acoustic analogy may lead to spurious noise at a high-frequency level [48].

In Fig. 19, the consistency of the SPL predictions in (very-)near field receivers (i.e., R-01, 02, 03 and 04) obtained using the FW-H method and DNC refers to the validity of the solution. The R-01 is positioned towards the slipstream, (-) x direction, and parallel to the rotation axis in the x-z plane to be close to the axial location of the actual hydrophone (8103) and radially (very-)near the linear source of the sound. The consistency of the noise spectra in the R-01 position provides a reliable solution, in a certain frequency range, regarding whether there is any spurious noise based on the end surfaces of the source that may dominate the pressure fluctuation towards the (-) x direction. As the distance from the acoustic source increased, both BPF (i.e., 100 Hz and its harmonics) tonal noise signatures faded away, and the discrepancy of predictions obtained by the FW-H method and DNC increased, probably due to discretisation errors and numerical dissipation (R-05 to 18).

The deviation of the FW-H acoustic analogy predictions was examined for the receivers defined along the x-y (R-09 and 13–15, R-10 and 16–18) and y-z (R-06 and 08, R-07 and 09) planes, having the same distance to the propeller centre, to assess the directivity. In Fig. 20, the predictions show no strong directivity both in x-y and x-z planes, as far as a certain frequency, [100, 1000] Hz, range is concerned. The end surfaces of the source may lead to a spurious noise at higher frequencies, especially in the x-y plane [48], but the time step size assigned regarding the frequency range concerned is not appropriate to assess the directivity above a certain frequency. The time step (Δt) size that refers to the sampling rate (f_s) and the maximum frequency (f_{max}) to be resolved accurately was assigned initially as 5.55×10^{-5} s, approximately equal to the $0.50°$ rotation of the propeller.

The predicted noise levels using the FW-H method and DNC in larger domain configuration refer to the solution's reliability and the FW-H method's requirement to obtain a reliable prediction at a position where the hydrophone (8103) was located in the experiments. However, predicting the noise level using the acoustic analogy in the same domain as the experiments having hard-wall boundary conditions is inconvenient due to the FW-H method's infinite domain assumption. Therefore, the receiver positions to extract the pressure fluctuations using the DNC were determined based on the FW-H method and DNC comparison in the larger domain configuration; then, the direct noise predictions were performed by modelling the cavitation tunnel's test section.

A comparison of the pressure fluctuations and the noise predictions obtained using the DNC in a larger domain and actual configuration is shown in Fig. 21. It is obvious that modelling the test section and, hence, having hard-wall boundary conditions reduces the pressure level at all receiver positions (i.e., R-01, 02, 03 and 04). This can be related to the influence of boundary layer displacement thickness based on the no-slip wall definition along the outer region of the computational domain. This has the impact of reducing the pressure level with a slight increase towards the near-wall region. The predicted noise levels in both configurations are found to be in satisfactory agreement due to the pressure fluctuations (characterised by its phase and amplitude) being analogous, even if the overall pressure level increases in the actual configuration. The phase average of the pressure distributions on the consecutive circular sections along the flow field and point sources in x, y and z directions are given in Figs. 22 and 23, respectively, certifying the impact of the actual configuration in a detailed arrangement.

The rest of the analyses were performed in the larger domain configuration to predict and compare the noise levels by the dynamic adaptive mesh refinement approach in non-cavitating and cavitating conditions. This is because the FW-H method is required to extract the pressure fluctuations at the hydrophone (8103) location in the experiments, and the predicted noise levels in both configurations (i.e., without and with modelling the cavitation tunnel's test section) agree. In addition, modelling the test section and
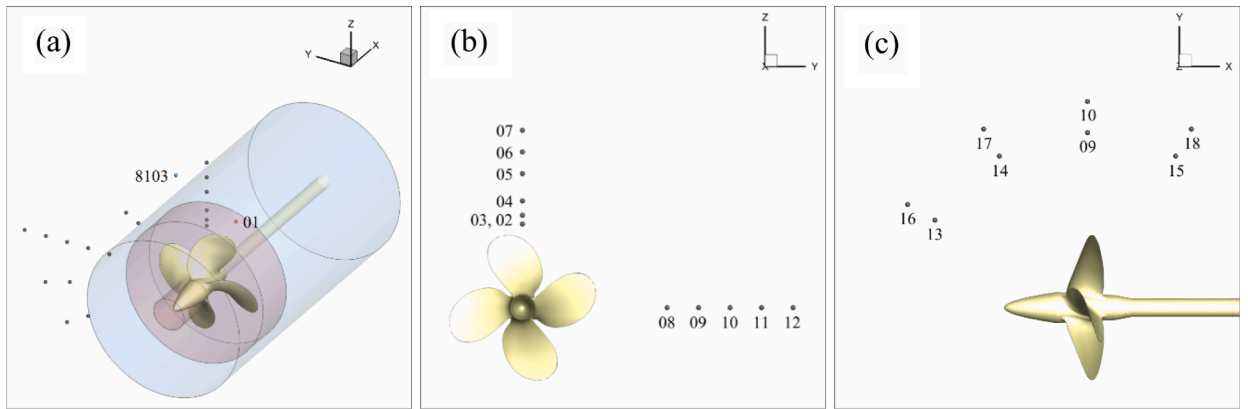
Fig. 18. Position of receivers in the simulations. (a) hydrophone (8103) location in the experiments and simulations, (b) receiver array along the propeller (i.e., *z-y*) plane, (c) receiver array along the *x-y* plane.
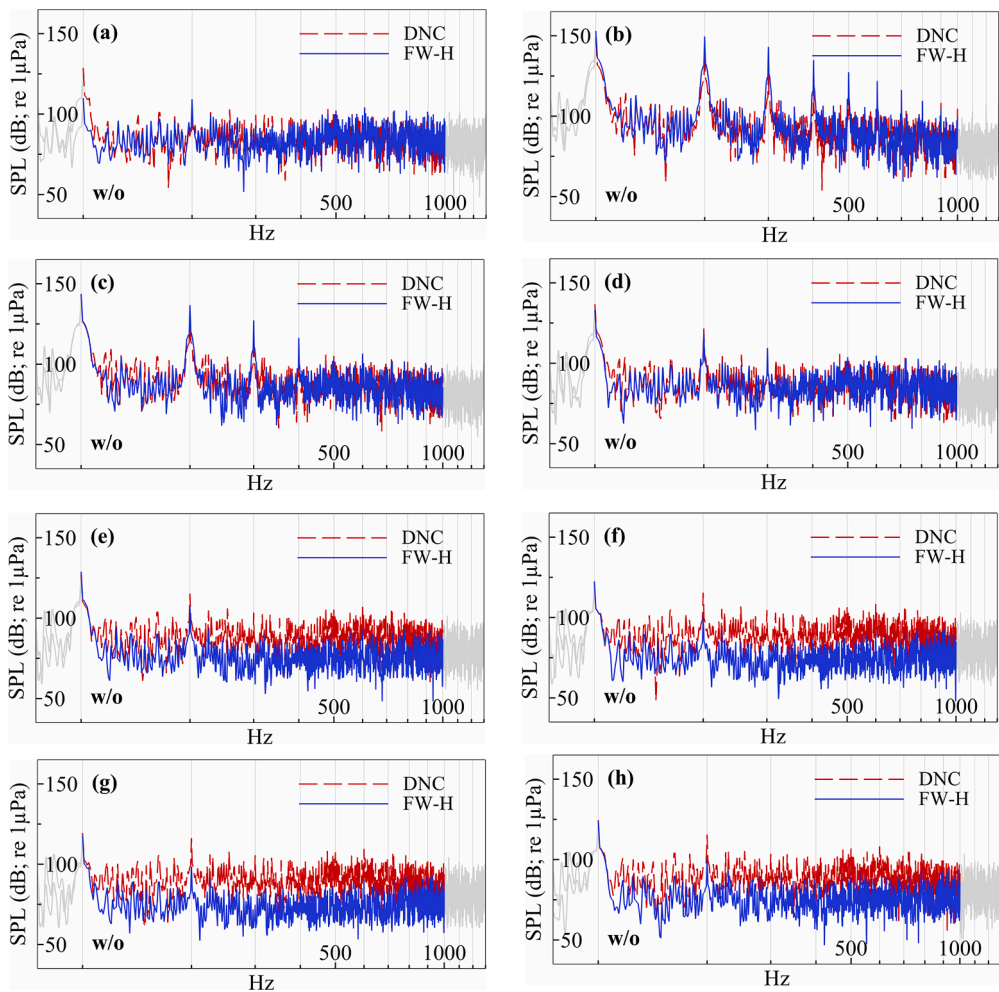
Fig. 19. Comparison of the noise predictions ($J = 0.39$ and $\sigma = 0.39$), using acoustic analogy (FW-H) and direct noise calculation. (a) Rec. 01, (b) Rec. 02, (c) Rec. 03, (d) Rec. 04, (e) Rec. 05, (f) Rec. 06, (g) Rec. 07, (h) Rec. 08.
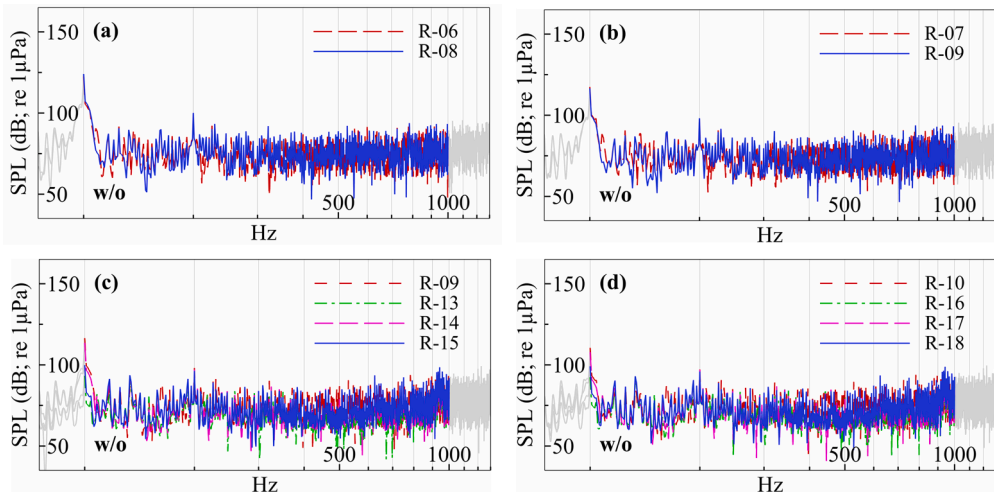
Fig. 20. Comparison of the noise predictions ($J = 0.39$ and $\sigma = 0.39$) using acoustic analogy (FW-H). (a) Rec. 06 and 08 along the *y-z* plane, (b) Rec. 07 and 09 along the *y-z* plane, (c) Rec. 09 and 13–15 along the *x-y* plane, (d) Rec. 10 and 16–18 along the *x-y* plane.
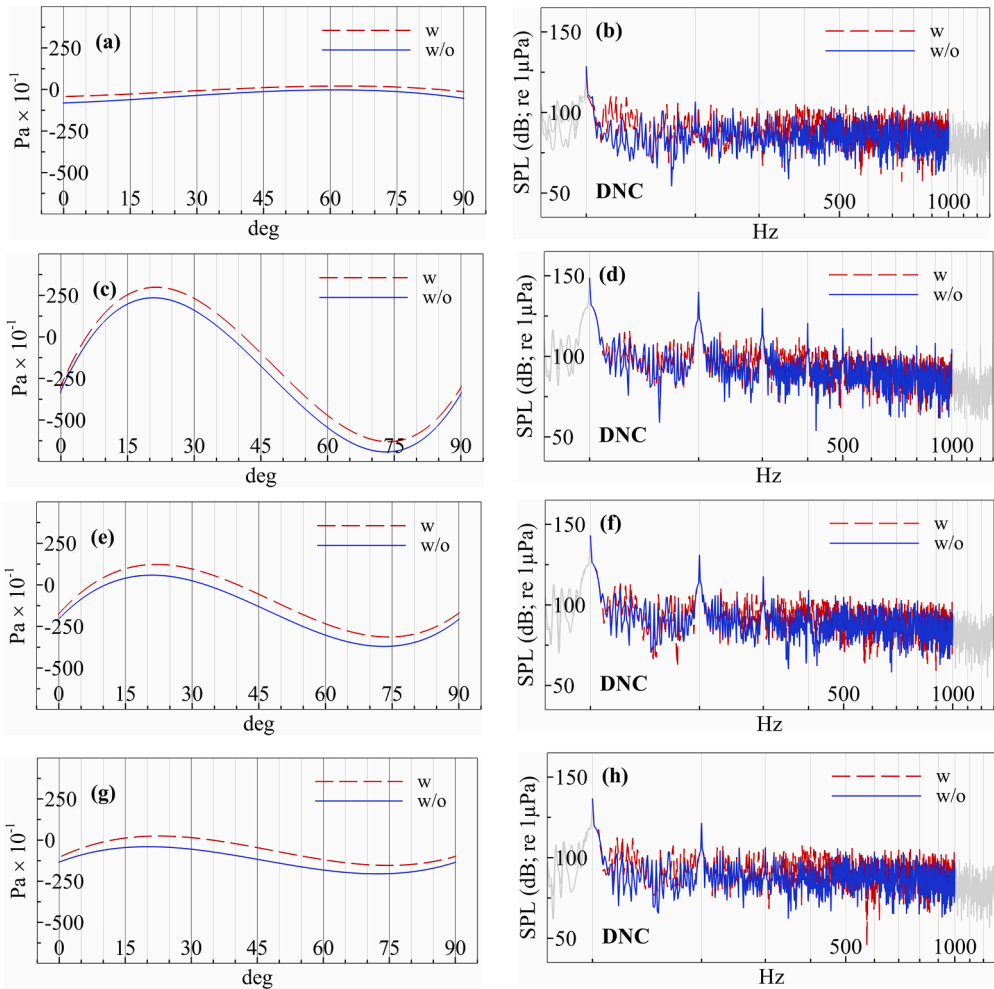
Fig. 21. Comparison of the pressure fluctuations and noise predictions ($J = 0.39$ and $\sigma = 0.39$) using direct noise calculation (DNC) without (w/o) and with (w) modelling the cavitation tunnel's test section. (a) Rec. 01, DNC, (b) Rec. 01, pressure fluctuations, (c) Rec. 02, DNC, (d) Rec. 02, pressure fluctuations, (e) Rec. 03, DNC, (f) Rec. 03, pressure fluctuations, (g) Rec. 04, DNC, (h) Rec. 04, pressure fluctuations.
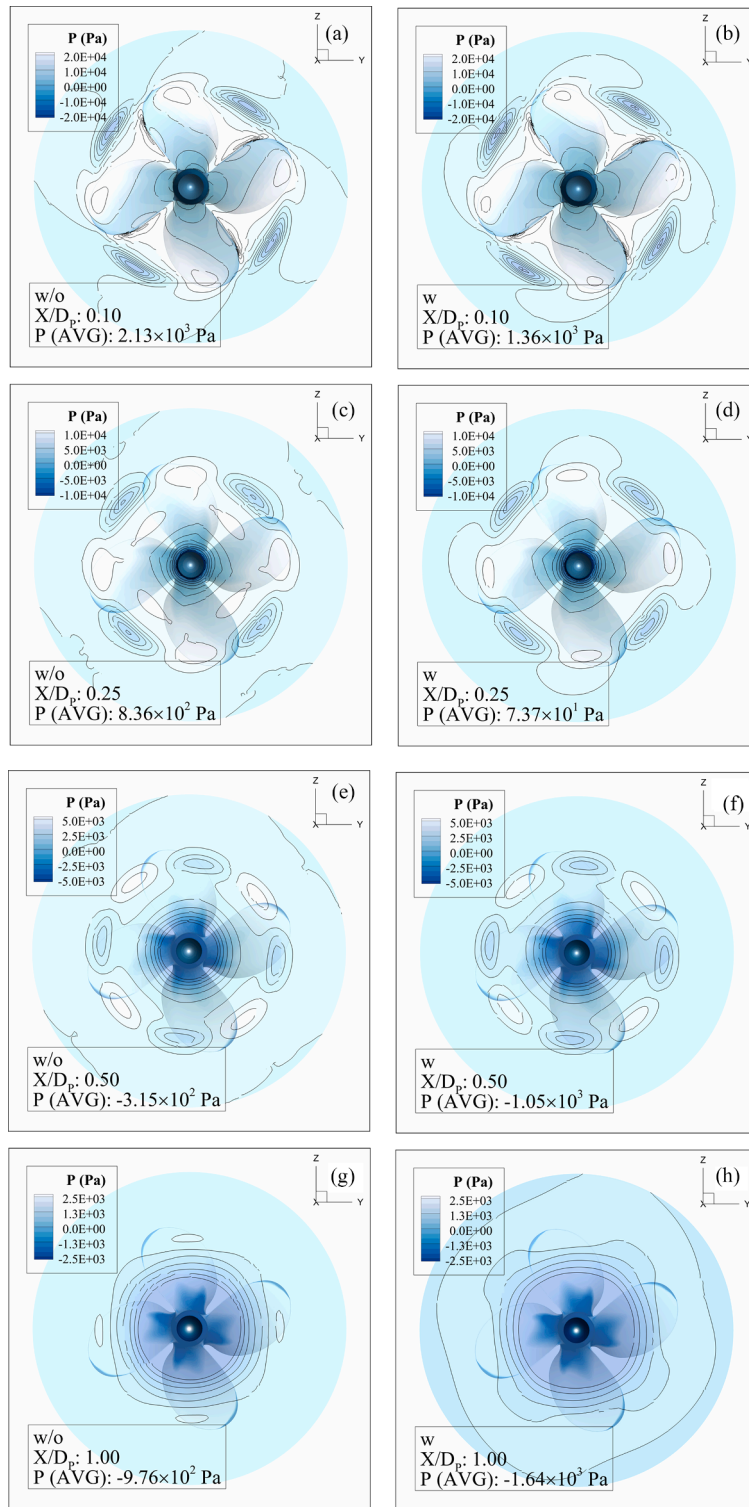
Fig. 22. The phase average of the pressure distributions on the consecutive circular sections along the flow field ($J = 0.39$ and $\sigma = 0.39$). (a) X/D$_P$: 0.10, w/o, (b) X/D$_P$: 0.10, w, (c) X/D$_P$: 0.25, w/o, (d) X/D$_P$: 0.25, w, (e) X/D$_P$: 0.50, w/o, (f) X/D$_P$: 0.50, w, (g) X/D$_P$: 1.00, w/o, (h) X/D$_P$: 1.00, w.

having hard-wall boundary conditions increase the total number of cells for the solution, not drastically but considerably. As a result, the numerical and experimental results were compared in non-cavitating conditions and were found to be in good agreement, as shown in Fig. 24.
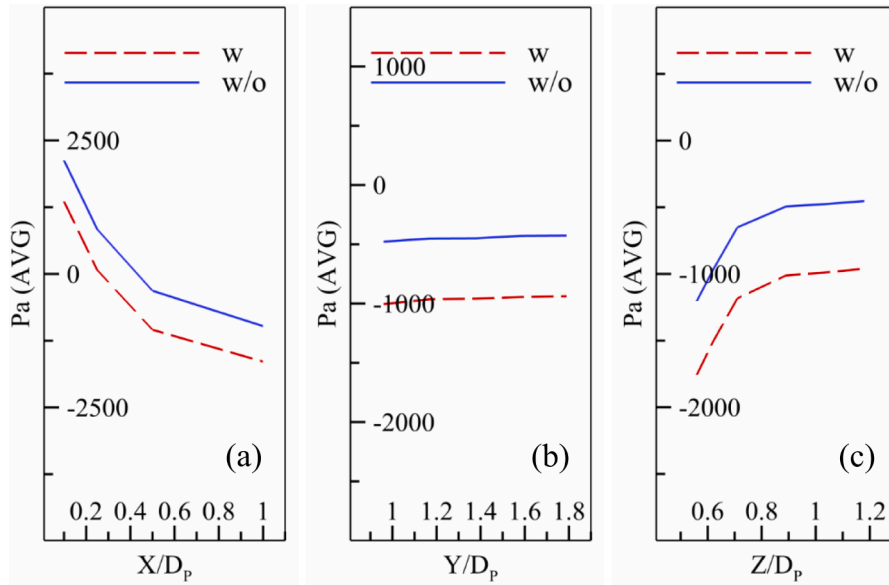
Fig. 23. The average of the pressure fluctuations on the point sources in (a) *x*, (b) *y* and (c) *z* directions ($J = 0.39$ and $\sigma = 0.39$).
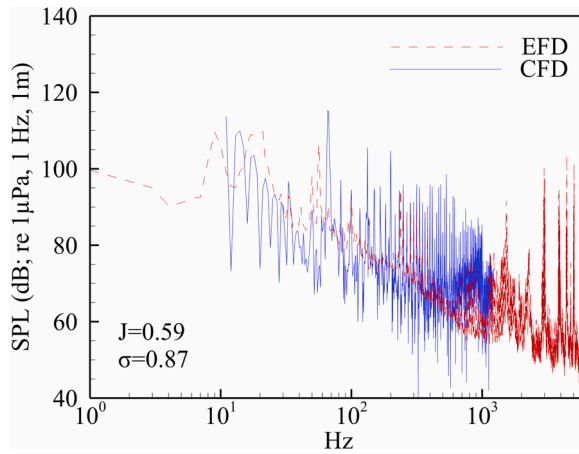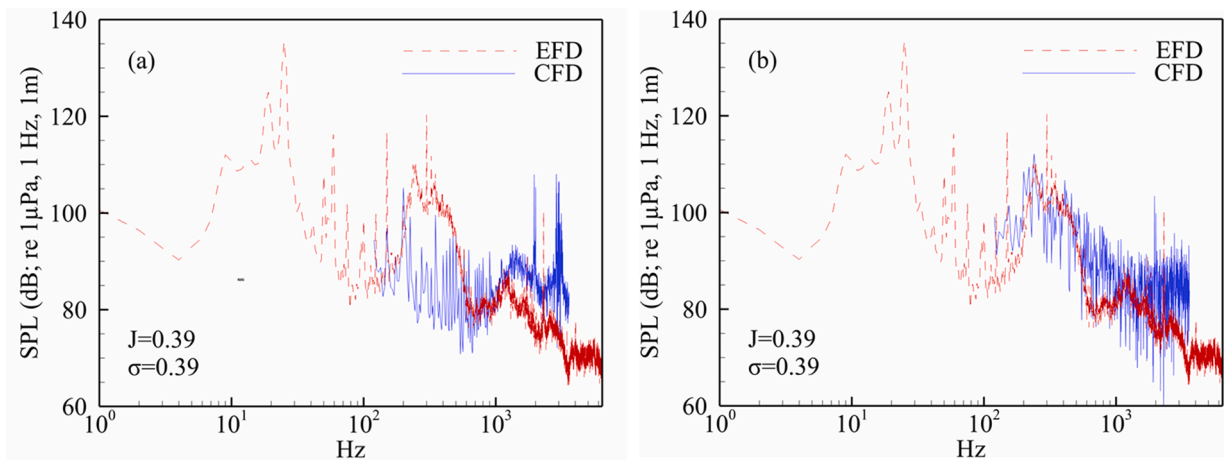

Fig. 24. Comparison of the noise spectrums in non-cavitating condition ($J = 0.59$ and $\sigma = 0.87$).

The experimental and numerical results were also compared in cavitating condition (Fig. 25). The noise prediction, Fig. 25(a), obtained without mesh refinement approach reveals that results are compatible with the measurements in a range of [100, 250] Hz and [500, 1000] Hz. However, within the broadband hump frequency, [250, 500] Hz, the numerical results mainly diverged due to the tip-vortex cavitation. Considering the prediction obtained by the dynamic adaptive mesh refinement approach, the results agree with the measurements, including the broadband hump frequency range, as in Fig. 25(b), demonstrating the importance of the tip vortex cavitation and its accurate prediction.

5. Conclusions

In this study, a numerical investigation into marine propeller's URN prediction was performed by introducing a dynamic adaptive mesh refinement approach to capture tip vortex cavitation dynamics for the first time. Based on the investigation, the following conclusions were drawn:

- The isocontours of the vapour volume fraction field caused by the cavitation were not included in the refinement region. Instead, the downstream was divided into several imaginary regions. The marked cells within each region along the downstream were adapted in four refinement levels, assigning an individual criterion on each level. Thus, the computational cost and the number of cells were considerably reduced.

Fig. 25. Comparison of the noise spectrums in non-cavitating conditions ($J = 0.39$ and $\sigma = 0.39$), (a) without mesh refinement, (b) by the dynamic adaptive mesh refinement.

- As the cell size was refined through the simulations, the time step also decreased to confirm the numerical stability, depending on the Courant-Friedrichs-Levy criteria (CFL $\leq$ 1).
- A hump shape pattern was observed in the noise spectra based on the cavitation inception. The broadband hump bandwidth shifted towards lower frequencies as the propeller loading increased. Therefore, broadband hump could not be associated with a specific frequency range.
- The comparison performed in the non-cavitating condition was compatible with the noise measurements. In the presence of cavitation, the tip-vortex cavitation was captured accurately when the dynamic adaptive mesh refinement strategy was implemented, compared to the case without its implementation. Moreover, the frequency range of the hump-shape pattern on the noise spectrum was correctly estimated. Consequently, if the tip-vortex cavitation formation would not be captured, an accurate noise spectrum estimation would be lacking.
- The impact of TVC modelling on the noise spectrum will be evaluated in further investigations, specifically in the behind-the-ship configuration, which is a challenging task to measure the capability of the proposed approach in predicting URN.

CRediT authorship contribution statement

Çağatay Sabri Köksal: Writing – original draft, Software, Methodology, Conceptualization. **Batuhan Aktas:** Writing – original draft, Visualization. **Mehmet Atlar:** Writing – review & editing, Resources. **Emin Korkut:** Writing – review & editing, Supervision.

Declaration of competing interest

The authors declare that they have no known competing financial interests or personal relationships that could have appeared to influence the work reported in this paper.

Data availability

Data will be made available on request.

Supplementary materials

Supplementary material associated with this article can be found, in the online version, at doi:10.1016/j.jsv.2024.118422.

References

[1] A.N. Popper, A. Hawkins. The effects of noise on aquatic life II 875, Springer, New York, 2016, https://doi.org/10.1007/978-1-4939-2981-8.

[2] L.S. Weilgart. The Impact of Ocean Noise Pollution on Marine Biodiversity, Dalhousie University, Halifax, 2008 [dissertation].

[3] L.S. Weilgart, Underwater noise: Death knell of our oceans?, Retrieved on July, 2004, 23, Available at: https://www.raincoast.org/library/wp-content/uploads/2011/05/weilgart_underwater-noise-death-knell.pdf, (Accessed March 14, 2024).

[4] IMO, IMO Marine Environment Protection Committee, Noise from Commercial Shipping and its Adverse Impact on Marine Life, Development of an International Standard for Measurement of Underwater Noise Radiated from Merchant Ships, 2011 MEPC 62/19, Available at: https://www.cbd.int/doc/meetings/mar/mcbem-2014-01/other/mcbem-2014-01-submission-imo-02-en.pdf, 2011, (Accessed March 31, 2024).

[5] IMO, IMO Marine Environment Protection Committee, AOB, Shipping Noise and Marine Mammals, 2007 MEPC 57/INF.4, Available at: https://www.gc.noaa.gov/documents/mepc_57_20_inf_4.pdf, 2007, (Accessed March 31, 2024).

[6] D. Ross, Propeller cavitation noise. Mechanics of Underwater Noise, Elsevier, California, 1976, pp. 253–287, https://doi.org/10.1016/B978-0-08-021182-4.50014-3.

[7] R.C. Leaper, M.R. Renilson, A review of practical methods for reducing underwater noise pollution from large commercial vessels, Trans. R. Inst. Nav. Archit. Part A Int. J. Marit. Eng. 156 (2014) 203–205, https://doi.org/10.5750/ijme.v156ia2.928. PART A2.

[8] J.E. Ffowcs Williams, D.L. Hawkings, Sound generation by turbulence and surfaces in arbitrary motion, Philos. Trans. R. Soc. Lond. Ser. A Math. Phys. Sci. 264 (1151) (1969) 321–342.

[9] F. Farassat, Theory of noise generation from moving bodies with an application to helicopter rotors, NASA TR R-451, 1975.

[10] C. Testa, S. Ianniello, F. Salvatore, A Ffowcs Williams and Hawkings formulation for hydroacoustic analysis of propeller sheet cavitation, J. Sound Vib. 413 (2018) 421–441, https://doi.org/10.1016/j.jsv.2017.10.004.

[11] A.K. Lidtke, T. Lloyd, F.H. Lafeber, J. Bosschers, Predicting cavitating propeller noise in off-design conditions using scale-resolving CFD simulations, Ocean Eng. 254 (April) (2022) 111176, https://doi.org/10.1016/j.oceaneng.2022.111176.

[12] A.K. Lidtke, V.F. Humphrey, S.R. Turnock, Feasibility study into a computational approach for marine propeller noise and cavitation modelling, Ocean Eng. 120 (2016) 152–159, https://doi.org/10.1016/j.oceaneng.2015.11.019.

[13] S. Sezen, M. Atlar, P. Fitzsimmons, N. Sasaki, G. Tani, N. Yilmaz, B. Aktas, Numerical cavitation noise prediction of a benchmark research vessel propeller, Ocean Eng. 211 (2020), https://doi.org/10.1016/j.oceaneng.2020.107549.

[14] A. Posa, M. Felli, R. Broglia, The signature of a propeller–rudder system: acoustic analogy based on LES data, Ocean Eng. 259 (April) (2022) 112059, https://doi.org/10.1016/j.oceaneng.2022.112059.

[15] A. Posa, R. Broglia, M. Felli, Acoustic signature of a propeller operating upstream of a hydrofoil, Phys. Fluids 34 (6) (2022), https://doi.org/10.1063/5.0096030.

[16] A. Posa, R. Broglia, M. Felli, M. Cianferra, V. Armenio, Hydroacoustic analysis of a marine propeller using large-eddy simulation and acoustic analogy, J. Fluid Mech. 947 (2022) 1–33, https://doi.org/10.1017/jfm.2022.692.

[17] R.E. Bensow, G. Bark, Implicit LES predictions of the cavitating flow on a propeller, J. Fluids Eng. Trans. ASME 132 (4) (2010) 0413021–04130210, https://doi.org/10.1115/1.4001342.

[18] M. Ge, U. Svennberg, R.E. Bensow, Investigations on prediction of ship noise using the FWH acoustic analogy with incompressible flow input, Ocean Eng. 257 (April) (2022) 111531, https://doi.org/10.1016/j.oceaneng.2022.111531.

[19] Ç.S. Köksal, O. Usta, B. Aktas, M. Atlar, E. Korkut, Numerical prediction of cavitation erosion to investigate the effect of wake on marine propellers, Ocean Eng. 239 (2021).

[20] R.E.A. Arndt, Cavitation in vortical flows, Annu. Rev. Fluid Mech. 34 (2002) 143–175, https://doi.org/10.1146/annurev.fluid.34.082301.114957.

[21] P. Pennings, J. Westerweel, T. van Terwisga, Cavitation tunnel analysis of radiated sound from the resonance of a propeller tip vortex cavity, Int. J. Multiph. Flow 83 (2016) 1–11, https://doi.org/10.1016/j.ijmultiphaseflow.2016.03.004.

[22] B. Aktas, M. Atlar, P. Fitzsimmons, W. Shi, An advanced joint time-frequency analysis procedure to study cavitation-induced noise by using standard series propeller data, Ocean Eng. 170 (May) (2018) 329–350, https://doi.org/10.1016/j.oceaneng.2018.10.026.

[23] A. Konno, K. Wakabayashi, H. Yamaguchi, M. Maeda, N. Ishii, S. Soejima, K. Kimura, On the mechanism of the bursting phenomena of propeller tip vortex cavitation, J. Mar. Sci. Technol. 6 (4) (2002) 181–192, https://doi.org/10.1007/s007730200006.

[24] N. Yilmaz, B. Aktas, M. Atlar, P.A. Fitzsimmons, M. Felli, An experimental and numerical investigation of propeller-rudder-hull interaction in the presence of tip vortex cavitation (TVC), Ocean Eng. 216 (2020), https://doi.org/10.1016/j.oceaneng.2020.108024.

[25] B. Aktas, A Systematic Experimental Approach to Cavitation Noise Prediction of Marine Propellers, Newcastle University, Newcastle Upon Tyne, 2016 [dissertation].

[26] J. Bosschers, Propeller Tip-Vortex Cavitation and Its Broadband Noise, University of Twente, Enschede, 2018 [dissertation].

[27] ITTC, ITTC specialist committee on hydrodynamic noise, in: Proceedings of the Final Report and Recommendations to the 27th International Towing Tank Conference, 2014.

[28] ITTC, ITTC quality systems group, in: Proceedings of the 28th International Towing Tank Conference, Recommended Procedures and Guidelines, Open Water Test, 2014, 7.5-02-03-02.1.

[29] ITTC, ITTC propulsion committee, in: Proceedings of the 27th International Towing Tank Conference, Recommended Procedures and Guidelines, Uncertainty Analysis, Example for Open Water Test, 2014, 7.5-02-03-02.2.

[30] ITTC, ITTC specialist committee on scaling of wake fields, in: Proceedings of the 26th International Towing Tank Conference, Recommended Procedures and Guidelines, Model Scale Cavitation Test, 2011, 7.5-02-03-03.1.

[31] ITTC, ITTC specialist committee on hydrodynamic noise, in: Proceedings of the 27th International Towing Tank Conference, Recommended Procedures and Guidelines, Model Scale Noise Measurements, 2014, 7.5-02-01-05.

[32] S. Secretariat, Quantities and Procedures for Description and Measurement of Underwater Sound from Ships – Part 1 :General Requirements, American National Standard, ANSI/ASA S, 2009.

[33] G. Tani, M. Viviani, J. Hallander, T. Johansson, E. Rizzuto, Propeller underwater radiated noise: a comparison between model scale measurements in two different facilities and full-scale measurements, Appl. Ocean Res. 56 (2016) 48–66.

[34] H. Tennekes, J.L. Lumley, A First Course in Turbulence, MIT, Cambridge, 1972, https://doi.org/10.7551/mitpress/3014.001.0001.

[35] J. Blazek, Computational Fluid Dynamics: Principles and Applications, 3rd ed., Elsevier, Oxford, 2001 https://doi.org/10.1016/C2013-0-19038-1.

[36] S.V. Patankar, D.B. Spalding, A calculation procedure for heat, mass and momentum transfer in three-dimensional parabolic flows, Int. J. Heat Mass Transf. 15 (1972) 1787–1806.

[37] L. Davidson, Numerical Methods for Turbulent Flow, MTF071 Lecture Notes, Chalmers University of Technology, Goteborg, Sweden, 2005. Department of Thermo and Fluid Dynamics.

[38] F.R. Menter, Y. Egorov, The scale-adaptive simulation method for unsteady turbulent flow predictions. part 1: theory and model description, J. Flow Turbul. Combust. 85 (2010) 113–138.

[39] C.C. Wang, B. Huang, G.Y. Wang, Z.P. Duan, B. Ji, Numerical simulation of transient turbulent cavitating flows with special emphasis on shock wave dynamics considering the water/vapor compressibility, J. Hydrodyn. 30 (6) (2018) 1–19.

[40] G.H. Schnerr, J. Sauer, Physical and numerical modelling of unsteady cavitation dynamic, in: Proceedings of the 4th International Conference on Multiphase Flow, New Orleans, USA, 2001.

[41] C.E. Brennen, Cavitation and Bubble Dynamics, Cambridge University Press, Cambridge, 2013, https://doi.org/10.1017/CBO9781107338760.

[42] K.S. Brentner, F. Farassat, Analytical comparison of the acoustic analogy and Kirchhoff formulation for moving surfaces, AIAA J. 36 (8) (1998) 1379–1386, 1998.

[43] ITTC, ITTC resistance committee, in: Proceedings of the 28th International Towing Tank Conference, Recommended Procedures and Guidelines, Uncertainty Analyses in CFD Verification and Validation, Methodology and Procedures, 2017, 7.5-03-01-01.

[44] ITTC, ITTC specialist committee on CFD in marine hydrodynamics, in: Proceedings of the 27th International Towing Tank Conference, Recommended Procedures and Guidelines, Practical Guidelines for Ship Self-Propulsion CFD, 2014, 7.5-03-03-01.

[45] R.E. Apfel, Acoustic cavitation prediction, J. Acoust. Soc. Am. 69 (6) (1981) 1624–1633.

[46] A. Shakeel, On the Noise Generated by a Ship Propeller, University of New South Wales, Sydney, 2020 [dissertation].

[47] S. Ianniello, E.D. Bernardis, Farassat's formulations in marine propeller hydroacoustics, Int. J. Aeroacoust. 14 (1–2) (2015) 87–103.

[48] M. Vikström, U. Svennberg, M. Ge, R.E. Bensow, The Effect of porous data surface shape and size on ship noise prediction using the FWH acoustic analogy with incompressible solver for a cavitating propellers, in: Proceedings of the 7th International Symposium of Marine Propulsors, Wuxi, China, 2022.

[49] D.Q. Li, J. Hallander, T. Johansson, R. Karlsson, Cavitation dynamics and underwater radiated noise signature of a ship with a cavitating propeller, in: Proceedings of the VI International Conference on Computational Methods in Marine Engineering, MARINE, 2015.

[50] S. Özsayan, Ç.S. Köksal, O. Usta, C. Çelik, N. Yılmaz, E. Korkut, An experimental and numerical investigation of the cavitation effects on propeller performance and erosion on DTMB-5415 propeller, in: Proceedings of the 7th International Symposium of Marine Propulsors, Wuxi, China, 2022.

[51] O. Usta, Ç.S. Köksal, E. Korkut, Systematic study into the cavitation erosion test for marine propeller materials by cavitating jet technique, Ocean Eng. 284 (2023).

[52] A. Posa, M. Felli, R. Broglia, Influence of an upstream hydrofoil on the acoustic signature of a propeller, Phys. Fluids 34 (4) (2022) 045112, https://doi.org/10.1063/5.0086633.

[53] Ç.S. Köksal, A.Y. Gürkan, B. Aktas, U.O. Ünal, P. Fitzsimmons, N. Sasaki, E. Korkut, M. Atlar, Quantifying the influence of Gate Rudder System (GRS) rudder angle(s) on propeller cavitation, Proceedings of the 8th International Symposium of Marine Propulsors, Berlin, Germany, 2024. 10.15480/882.9364.